

Fundamental Limits and Optimization of Multiband Sensing

Yubo Wan, *Graduate Student Member, IEEE*, An Liu, *Senior Member, IEEE*, Rui Du, and Tony Xiao Han, *Senior Member, IEEE*

Abstract

Multiband sensing is a promising technology that utilizes multiple non-contiguous frequency bands to achieve high-resolution target sensing. However, rare studies have investigated the fundamental limits and optimization of multiband sensing systems. In this paper, we investigate the fundamental limits and optimization of multiband sensing, focusing on the fundamental limits associated with time delay. We first derive a closed-form expression of the Cramér-Rao bound (CRB) for the delay separation to reveal useful insights. Then, a metric called the statistical resolution limit (SRL) that provides a resolution limit is employed to investigate the fundamental limits of delay resolution. The fundamental limits of delay estimation are also investigated based on the CRB and Ziv-Zakai bound (ZZB). Based on the above derived fundamental limits, numerical results are presented to analyze the effect of frequency band apertures and phase distortions on the performance limits of the multiband sensing systems. Inspired by the fundamental limits analysis, we formulate an optimization problem to find the optimal system configuration in multiband sensing systems with the objective of minimizing the delay SRL. To solve this non-convex constrained problem, we propose an efficient alternating optimization (AO) based algorithm which iteratively optimizes the variables using successive convex approximation (SCA) and one-dimensional search. Simulation results demonstrate the effectiveness of the proposed algorithm.

Index Terms

Multiband, target sensing, statistical resolution limit, Cramér-Rao bound, Ziv-Zakai bound, fundamental limits.

I. INTRODUCTION

Using wireless systems for target sensing has sparked considerable interests in the recent years, and it fosters a wide range of emerging applications such as indoor localization [1], [2], activity recognition [3], [4], [5], and integrated sensing and communication (ISAC) [6], [7], [8], etc. To achieve high-accuracy target sensing, these applications need to rely on the channel state information (CSI), which reveals important information about the multipath propagation environment.

However, the target sensing performance is limited by the delay resolution, which is inversely proportional to the bandwidth of the transmitted signal. To address this issue, the multiband technology is proposed, which provides the potential to achieve high-resolution target sensing by making use of the CSI measurements across multiple non-contiguous frequency bands. As shown in Fig. 1, the spectrum resource used for target sensing consists of a

This work was supported in part by National Science Foundation of China (No.62071416), and in part by Huawei Technologies Co., Ltd. (Corresponding authors: An Liu.)

Yubo Wan and An Liu are with the College of Information Science and Electronic Engineering, Zhejiang University, Hangzhou 310027, China (email: wanyb@zju.edu.cn; anliu@zju.edu.cn).

Tony Xiao Han and Rui Du are with Huawei Technologies Co., Ltd. (email: tony.hanxiao@huawei.com).

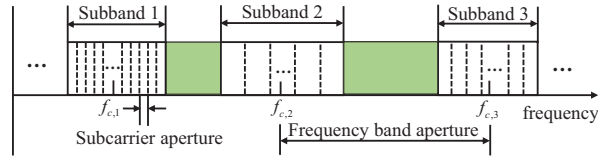


Fig. 1. The frequency distribution of the multiband sensing systems.

number of subbands in the presence of frequency band apertures, where $f_{c,1}$, $f_{c,2}$, and $f_{c,3}$ are carrier frequencies. The frequency subbands allocated to other systems are illustrated by the green color, which cannot be utilized for target sensing. A few multiband based sensing algorithms have been proposed recently, which achieve high-accuracy multipath channel delay estimation for ranging and localization, and illustrate that the improvement of estimation accuracy is brought by the frequency band apertures [9], [10], [11], [12], [13], [14].

It is well known that fundamental limits not only serve as a performance bound for practical multiband sensing technologies, but may also provide useful guidance and insights for the design and analysis of multiband sensing systems. However, the fundamental limits of a multiband based sensing problem have not been fully investigated, especially under the practical consideration of the phase distortions caused by hardware imperfections [15], [16], [17]. Only a few studies have investigated the effect of frequency band apertures on delay resolution and delay estimation accuracy based on a fundamental limit analysis. In [12], [18], the Cramér-Rao bound (CRB) is derived for the delay estimation error based on a multiband signal model. However, there are several limitations: (i) The authors only empirically showed that the CRB decreases with the increase of frequency band apertures via numerical simulations without a theoretical analysis; (ii) The effect of phase distortions is not considered; (iii) The CRB is a local bound, which may not be tight over a wide range of frequency band apertures. In [19], the authors derived the closed-form expression of the statistical resolution limit (SRL) based on a simple pole model and showed the effect of band apertures on the resolution. The SRL is defined as the source separation that equals its own root squared CRB, which provides a performance bound on the resolution of any practical method. However, the derived results are restricted to a simple pole model and have approximation errors. Hence, in the aforementioned studies, detailed effects of frequency band apertures and phase distortions on the fundamental limits of delay estimation and delay resolution remain underexplored.

Besides, determining how to improve the delay resolution limit by designing the system parameters (e.g., the carrier frequency and the number of subcarriers for each subband) in multiband sensing systems is another challenging problem. To the best of our knowledge, there is little literature refers to designing the multiband sensing system parameters at the transmitter for the purpose of improving the sensing performance limits. In [20], the authors proposed a sparse subbands selection methodology for ranging based on the CRB. However, it only involves subbands selection with fixed system parameters. In addition, the path gain variables are assumed to be real, which is restrictive. In [21], the authors investigated a problem of multiple subarrays geometry design, which is similar to the optimization problem of multiband sensing. However, they only considered a simplified optimization problem of minimizing the CRB for a single source DOA estimation and did not investigate the fundamental limits

in terms of SRL or ZZB.

In this paper, we study the effect of frequency band apertures and phase distortions on the multiband target sensing systems based on a comprehensive fundamental limit analysis, which is the key in understanding the multiband sensing systems. The Fisher information matrix (FIM) based on a practical multiband signal model is derived first, where the signal model considers the phase distortions, e.g., receiver timing offset and random phase offset. Then, we reformulate the FIM into a compact form using the Dirichlet kernel [22] to derive a closed-form expression of the CRB for the delay separation in a simplified case to reveal useful insights. Besides, numerical analyses are presented employing the metric SRL, that provides a fundamental limit of delay resolution in the presence of phase distortions. The performance bounds CRB and Ziv-Zakai bound (ZZB) are derived to analyze the fundamental limits of delay estimation, where the ZZB is a global bound computed by transforming the estimation problem to a binary hypothesis testing problem [23], [24], [25]. From the fundamental limits analysis, we have the following key insights: (1) The CRB for delay separation decreases with the increase of frequency band apertures in a square order; (2) Increasing the frequency band apertures leads to an improvement of delay resolution limit and the phase distortions have relatively slight interference on SRL; (3) The phase distortions degrade the performance limits of delay estimation and make it difficult to exploit the delay estimation performance gain brought by the frequency band apertures. However, when the targets are distinguishable with significantly different time delay and amplitudes, the negative effect of phase distortions can be suppressed; (4) ZZB provides a tighter bound than CRB over a wide range of frequency band apertures. Furthermore, the ZZB predicts a threshold behavior of a maximum a posteriori (MAP) estimator, i.e., the ZZB decreases first and then increases with the increase of frequency band apertures, which is consistent with the MAP estimation results.

Inspired from the above analyses, an optimization problem is formulated to find the optimal system configuration in multiband sensing systems, where the carrier frequency and the subcarrier number of each subband are jointly designed to minimize the delay SRL under the total bandwidth constraint. Besides, the carrier frequencies of all subbands are respectively constrained within a certain frequency interval to reflect the practical constraints that only a few non-contiguous subbands are available for target sensing. The formulated problem is difficult to solve since it has a non-convex equality constraint associated to the definition of SRL. Furthermore, the optimization variable, subcarrier number, is integer with the form of summation terms in the CRB expression, which is difficult to optimize. To overcome these challenges, we relax the integer variable to a real variable and employ the Dirichlet kernel to compactly reformulate the summation terms. Then, we adopt alternating optimization (AO) algorithms to alternatively optimize the variables of delay separation and system parameters. For given system parameters, the optimal delay SRL can be found by one-dimensional search of the delay separation. For given delay separation, the system parameters are optimized to minimize the CRB of the delay separation. We adopt the successive convex approximation (SCA) algorithm to solve this non-convex subproblem. Finally, the convergence of the overall algorithm has been proved. Numerical results are provided to validate the effectiveness of our proposed algorithms and present useful guidance for the system design.

The rest of this paper is organized as follows. Section II presents the system model and the derivations of the FIM. In Section III, we derive a closed-form expression of the CRB for delay separation. Then we introduce the

SRL and analyze the fundamental limits of delay resolution. Section IV studies the fundamental limits of delay estimation based on the derivation of the CRB and ZZB. Section V formulates a multiband sensing optimization problem and an efficient algorithm is proposed based on AO method. Finally, Section VI concludes the paper.

Notations: \mathbf{I} denotes an identity matrix, \propto denotes equality up to irrelevant constants, $\delta(\cdot)$ denotes the Dirac's delta function, $\text{diag}(\cdot)$ constructs a diagonal matrix from its vector argument, and $\|\cdot\|$ denotes the Euclidean norm of a complex vector. For a matrix A , A^T , A^H , A^{-1} represent a transpose, complex conjugate transpose, and inverse of a matrix, respectively. $\mathbb{E}_{\mathbf{z}}[\cdot]$ denotes the expectation operator with respect to the random vector \mathbf{z} . The notations \mathbb{R}^+ represents the strictly positive real number and $\mathcal{CN}(\boldsymbol{\mu}, \boldsymbol{\Sigma})$ denotes a complex Gaussian normal distribution with mean $\boldsymbol{\mu}$ and covariance matrix $\boldsymbol{\Sigma}$.

II. SYSTEM MODEL AND FIM

A. System Model

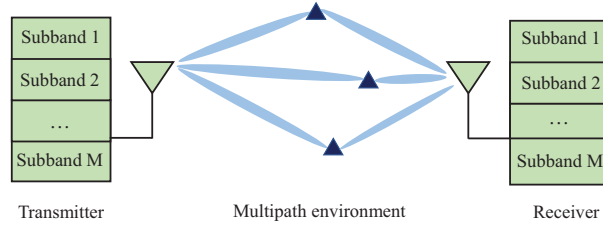


Fig. 2. An illustration of the multiband target sensing system.

As shown in Fig. 2, we consider a single-input single-output (SISO) multiband target sensing system which employs orthogonal frequency division multiplexing (OFDM) training signals over M frequency subbands. Note that the **multiband** sensing is mainly used to improve the delay resolution and a SISO system is sufficient to reveal the key insights on the fundamental limits of **multiband** sensing in terms of delay resolution/estimation. Then, the continuous-time channel impulse response (CIR) $h(t)$ can be written as [5]

$$h(t) = \sum_{k=1}^K \alpha_k \delta(t - \tau_k), \quad (1)$$

where K denotes the number of multipath caused by the scatters (targets) in the sensing environment between the transmitter and the receiver, $\alpha_k \in \mathbb{C}$ denotes a complex scalar carrying the amplitude and phase information of the k -th scatter, and $\tau_k \in \mathbb{R}^+$ denotes the time delay carrying the range information of the k -th scatter. The delays are sorted in an increasing order, i.e., $\tau_{k-1} < \tau_k$, $k = 2, \dots, K$. As in [10], [11], [12], we assume that $\alpha_k, \forall k$ and $\tau_k, \forall k$ are independent of the frequency subbands, and denote that each subband has N_m orthogonal subcarriers with subcarrier spacing $f_{s,m}$. The carrier frequency of the m -th subband is denoted as $f_{c,m}$. Then, via a Fourier transform of the CIR as in [12], the channel frequency response (CFR) samples can be expressed as

$$\tilde{h}_{m,n} = \sum_{k=1}^K \alpha_k e^{-j2\pi f_{m,n} \tau_k}, \quad (2)$$

where $f_{m,n} = f_{c,m} + n f_{s,m}$, $m = 1, \dots, M$, $n \in \mathcal{N}_m \triangleq \{-\frac{N_m-1}{2}, \dots, \frac{N_m-1}{2}\}$. We assume that $N_m, \forall m$ is an even number without loss of generality, and denote $N = N_1 + \dots + N_M$ as the number of CFR samples over all subbands. Then, during the period of a single OFDM symbol, the discrete-time received signal model can be written as [10], [11]

$$y_{m,n} = \sum_{k=1}^K \alpha_k e^{-j2\pi f_{m,n} \tau_k} e^{-j2\pi n f_{s,m} \delta_m} e^{j\varphi_m} s_{m,n} + w_{m,n}, \quad (3)$$

where $w_{m,n}$ is the n -th element of the additive white Gaussian noise (AWGN) vector $\mathbf{w}_m \in \mathbb{C}^{N_m \times 1}$, following the distribution $\mathcal{CN}(0, \sigma_{ns}^2 \mathbf{I})$. $s_{m,n}$ denotes a known training symbol over the n -th subcarrier of the m -th subband with the power $|s_{m,n}|^2 = 1$. The parameters φ_m and δ_m represent the phase distortions caused by random phase offset and receiver timing offset [15], [16], [17], respectively. In practice, the receiver timing offset δ_m is often within a small range and thus we assume that $\delta_m, \forall m$ follows a prior distribution $p(\delta_m) \sim \mathcal{N}(0, \sigma_p^2)$, where σ_p is the timing synchronization error. Note that the multiband system model has some similarities with the models used in multiple subarrays signal processing, e.g., [26]. However, the signal model used in [26] assumes that each subarray is perfectly calibrated, while in our formulated multiband signal model, each subband is not “perfectly calibrated” due to the effect of δ_m .

The received signal model (3) cannot be directly used for the fundamental limit analysis due to the inherent ambiguity. Specifically, for an arbitrary constant c , if we substitute two sets of variables ($|\alpha_k| e^{j\angle\alpha_k}, \varphi_m$) and ($|\alpha_k| e^{j(\angle\alpha_k+c)}, \varphi_m - c$) into (3), the same observation result will be obtained. It indicates that the parameters (α_k, φ_m) are ambiguous, which will result in a singular FIM [27]. Therefore, we equivalently transform the signal model (3) by absorbing the phase φ_1 and center frequency $f_{c,1}$ of the first subband as [13]

$$y_{m,n} = \mu_{m,n} + w_{m,n}, \quad (4)$$

where

$$\mu_{m,n} = \sum_{k=1}^K \alpha'_k e^{-j2\pi f'_{c,m} \tau_k} e^{-j2\pi n f_{s,m} \tau_k} e^{-j2\pi n f_{s,m} \delta_m} e^{j\varphi'_m} s_{m,n},$$

$f'_{c,m} = f_{c,m} - f_{c,1}$, $\alpha'_k = \alpha_k e^{j\varphi_1} e^{-j2\pi f_{c,1} \tau_k}$, and $\varphi'_m = \varphi_m - \varphi_1, \forall k, m$. The new signal model (4) eliminates the inherent ambiguity and reserves the structure of frequency band apertures, i.e., $e^{-j2\pi f'_{c,m} \tau_k}$. Note that it is more convenient to define the frequency band aperture as $f'_{c,m} = f_{c,m} - f_{c,1}$ instead of the entire frequency span because the fundamental limits such as CRB can be expressed as a function of $f'_{c,m}$'s. The proof of parameter identifiability of signal model (5) can be found in Appendix A.

B. FIM Derivation

Let $\boldsymbol{\eta} = [\boldsymbol{\tau}^T, \boldsymbol{\alpha}^T, \boldsymbol{\varphi}^T, \boldsymbol{\delta}^T]^T \in \mathbb{R}^{3K+2M-1}$ be the vector consisting of the unknown parameters, where

$$\begin{aligned}
\boldsymbol{\tau} &= [\tau_1, \tau_2, \dots, \tau_K]^T, \\
\boldsymbol{\alpha} &= [\boldsymbol{\alpha}_R^T, \boldsymbol{\alpha}_I^T]^T, \\
\boldsymbol{\alpha}_R &= [\alpha_{R,1}, \alpha_{R,2}, \dots, \alpha_{R,K}]^T, \\
\boldsymbol{\alpha}_I &= [\alpha_{I,1}, \alpha_{I,2}, \dots, \alpha_{I,K}]^T, \\
\boldsymbol{\varphi} &= [\varphi'_2, \dots, \varphi'_M]^T, \\
\boldsymbol{\delta} &= [\delta_1, \dots, \delta_M]^T,
\end{aligned} \tag{5}$$

in which $\alpha_{R,k}$ and $\alpha_{I,k}$ denote the real and imaginary parts of α'_k , respectively. Defining $\hat{\boldsymbol{\eta}}$ as the unbiased estimator of $\boldsymbol{\eta}$ based on the multiband observations

$$\mathbf{y} = \left[y_{1, -\frac{N_m-1}{2}}, \dots, y_{M, \frac{N_m-1}{2}} \right]^T \in \mathbb{C}^{N \times 1}. \tag{6}$$

Then, the mean squared error (MSE) matrix of $\hat{\boldsymbol{\eta}}$ satisfies the information inequality [28], [29]

$$\mathbb{E}_{\mathbf{y}, \boldsymbol{\delta}} [(\hat{\boldsymbol{\eta}} - \boldsymbol{\eta})(\hat{\boldsymbol{\eta}} - \boldsymbol{\eta})^T] \succeq \mathbf{J}_{\boldsymbol{\eta}}^{-1}, \tag{7}$$

where $\mathbf{J}_{\boldsymbol{\eta}}$ denotes the $(3K + 2M - 1) \times (3K + 2M - 1)$ FIM with a priori knowledge of $\boldsymbol{\delta}$, defined as

$$\begin{aligned}
\mathbf{J}_{\boldsymbol{\eta}} &= \mathbf{J}_w + \mathbf{J}_p, \\
\mathbf{J}_w &\triangleq \mathbb{E}_{\mathbf{y}, \boldsymbol{\delta}} \left[-\frac{\partial^2 \ln f(\mathbf{y}|\boldsymbol{\eta})}{\partial \boldsymbol{\eta} \partial \boldsymbol{\eta}^T} \right], \\
\mathbf{J}_p &\triangleq \mathbb{E}_{\boldsymbol{\delta}} \left[-\frac{\partial^2 \ln f(\boldsymbol{\delta})}{\partial \boldsymbol{\eta} \partial \boldsymbol{\eta}^T} \right],
\end{aligned} \tag{8}$$

where \mathbf{J}_w and \mathbf{J}_p are the FIMs from the observations and the a priori knowledge of $\boldsymbol{\delta}$, respectively. $f(\mathbf{y}|\boldsymbol{\eta}) \propto \exp\{-\frac{\|\mathbf{y}-\boldsymbol{\mu}\|_2^2}{\sigma_{ns}^2}\}$ is the likelihood function of the random vector \mathbf{y} conditioned on $\boldsymbol{\eta}$ and $f(\boldsymbol{\delta}) \propto \exp\{-\frac{\|\boldsymbol{\delta}\|_2^2}{2\sigma_\delta^2}\}$ is the prior distribution of $\boldsymbol{\delta}$, where $\boldsymbol{\mu} = [\mu_{1, -(N_m-1)/2}, \dots, \mu_{M, (N_m-1)/2}]^T \in \mathbb{C}^{N \times 1}$. The FIM $\mathbf{J}_{\boldsymbol{\eta}}$ can be structured as

$$\mathbf{J}_{\boldsymbol{\eta}} = \begin{bmatrix} \Psi(\boldsymbol{\tau}, \boldsymbol{\tau}) & \Psi(\boldsymbol{\tau}, \boldsymbol{\alpha}) & \Psi(\boldsymbol{\tau}, \boldsymbol{\varphi}) & \Psi(\boldsymbol{\tau}, \boldsymbol{\delta}) \\ \Psi(\boldsymbol{\alpha}, \boldsymbol{\tau}) & \Psi(\boldsymbol{\alpha}, \boldsymbol{\alpha}) & \Psi(\boldsymbol{\alpha}, \boldsymbol{\varphi}) & \Psi(\boldsymbol{\alpha}, \boldsymbol{\delta}) \\ \Psi(\boldsymbol{\varphi}, \boldsymbol{\tau}) & \Psi(\boldsymbol{\varphi}, \boldsymbol{\alpha}) & \Psi(\boldsymbol{\varphi}, \boldsymbol{\varphi}) & \Psi(\boldsymbol{\varphi}, \boldsymbol{\delta}) \\ \Psi(\boldsymbol{\delta}, \boldsymbol{\tau}) & \Psi(\boldsymbol{\delta}, \boldsymbol{\alpha}) & \Psi(\boldsymbol{\delta}, \boldsymbol{\varphi}) & \Psi(\boldsymbol{\delta}, \boldsymbol{\delta}) \end{bmatrix}, \tag{9}$$

where the entries of $\mathbf{J}_{\boldsymbol{\eta}}$ are derived in Appendix B.

From (41), we can observe that the FIM $\mathbf{J}_{\boldsymbol{\eta}}$ depends on the relative delay, e.g., $\tau_2 - \tau_1$, rather than on the absolute delay, which agrees with the results of [20], but the phase distortions are not considered in their model. Besides, though the FIM $\mathbf{J}_{\boldsymbol{\eta}}$ includes the entries associated with phase distortion factors $\boldsymbol{\delta}$ and $\boldsymbol{\varphi}$, it is independent of the value of $\boldsymbol{\delta}$ and $\boldsymbol{\varphi}$.

For clarity, an overview of the main contents and corresponding assumptions are summarized in Table I. The

TABLE I
AN OVERVIEW OF THE MAIN CONTENTS AND ADOPTED BASIC ASSUMPTIONS IN THE PAPER.

Section	II-B	III-A	III-B	IV-A	IV-B	V
Contents	FIM	Closed-form CRB	SRL	DEB	ZZB	System optimization
Basic Assumptions	Exist phase distortions	(i) Exist phase distortions (ii) $\alpha'_1 = \alpha'_2 = 1$	Exist phase distortions	Exist phase distortions	(i) Without phase distortions (ii) $K=1$	(i) Exist phase distortions (ii) Coarse estimation of α_k 's and K

different assumptions adopted in different sections are just special cases of the same general system model in (4). The purpose of considering these special cases is to highlight the impact of different system imperfections/parameters on the performance and to reveal useful insight that cannot be easily obtain in the general case.

III. FUNDAMENTAL LIMITS OF DELAY RESOLUTION

In this section, we consider a scenario with the number of subbands $M = 2$ and multipath number $K = 2$, since the delay resolution reflects the ability of resolving two paths with a small delay gap. Generally, the derivation of CRB involves a complicated high-dimensional matrix inverse operation. Hence, we derive a closed-form expression of the CRB for the delay separation in a special case to reveal useful insight. Finally, we investigate the fundamental limits of delay resolution employing the metric SRL.

A. The Closed-form CRB for the Delay Separation

To derive the closed-form expression of CRB for the delay separation, which is defined as $\Delta\tau = |\tau_2 - \tau_1|$, we need to reformulate the expression of FIM in (41) into a compact form by employing the Dirichlet kernel [22]. The details are elaborated in Appendix C.

Subsequently, the CRB for the delay separation in the presence of phase distortions is given by

$$\begin{aligned}
 C_{\Delta\tau} &= \frac{\partial \Delta\tau^T}{\partial \boldsymbol{\eta}} \mathbf{C}_{\boldsymbol{\eta}} \frac{\partial \Delta\tau}{\partial \boldsymbol{\eta}} \\
 &= \mathbf{C}_{\boldsymbol{\eta}}(1,1) + \mathbf{C}_{\boldsymbol{\eta}}(2,2) - \mathbf{C}_{\boldsymbol{\eta}}(1,2) - \mathbf{C}_{\boldsymbol{\eta}}(2,1),
 \end{aligned} \tag{10}$$

where $\mathbf{C}_{\boldsymbol{\eta}} = \mathbf{J}_{\boldsymbol{\eta}}^{-1}$ is the CRB associated with the vector $\boldsymbol{\eta}$. Particularly, we assume that $\sigma_{ns}^2 = 2$, $f_{s,1} = f_{s,2} = f_s$, $N_1 = N_2 = \bar{N}$, the amplitudes and phases of the two paths are set as $a_1 = a_2 = 1$ and $\phi_1 = \phi_2 = 0$ for simplicity. As can be seen, determining $C_{\Delta\tau}$ requires inverting the high-dimensional FIM $\mathbf{J}_{\boldsymbol{\eta}}$, while only a small submatrix $[\mathbf{J}_{\boldsymbol{\eta}}^{-1}]_{2 \times 2}$ is of interest. To circumvent high-dimensional matrix inversion, we introduce the equivalent FIM (EFIM) [30]. Given parameters $\boldsymbol{\theta}_1 = [\tau_1, \tau_2]^T$ and the FIM $\mathbf{J}_{\boldsymbol{\eta}}$ with the block matrix form

$$\mathbf{J}_{\boldsymbol{\eta}} = \begin{bmatrix} \mathbf{A} & \mathbf{B} \\ \mathbf{B}^T & \mathbf{C} \end{bmatrix}, \tag{11}$$

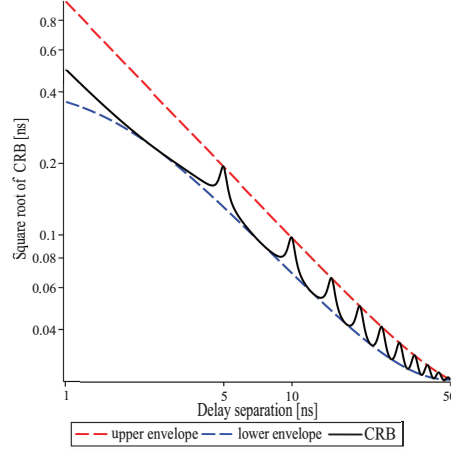


Fig. 3. An illustration of $C_{\Delta\tau}$ versus delay separation.

where $\mathbf{A} \in \mathbb{R}^{2 \times 2}$, $\mathbf{B} \in \mathbb{R}^{2 \times 7}$, $\mathbf{C} \in \mathbb{R}^{7 \times 7}$, the EFIM can be written as

$$\mathbf{J}_e(\boldsymbol{\theta}_1) \triangleq \mathbf{A} - \mathbf{B}\mathbf{C}^{-1}\mathbf{B}^T. \quad (12)$$

Since $[\mathbf{J}_\eta^{-1}]_{2 \times 2} = \mathbf{J}_e^{-1}(\boldsymbol{\theta}_1)$, (10) can be rewritten as

$$C_{\Delta\tau} = \mathbf{J}_e^{-1}(1, 1) + \mathbf{J}_e^{-1}(2, 2) - \mathbf{J}_e^{-1}(1, 2) - \mathbf{J}_e^{-1}(2, 1). \quad (13)$$

Finally, we can obtain a closed-form expression of $C_{\Delta\tau}$ using symbolic algebra packages. However, it is difficult to directly obtain insights from the closed-form expression due to its complicated structure. Hence, we turn to obtain the tight lower and upper bound of $C_{\Delta\tau}$, which are given by

$$\begin{aligned} \text{CRB}_{\text{up}} &= \frac{3\bar{N} + 3\gamma}{(\bar{N} + \gamma)(3\bar{N} - 3\gamma)\pi^2 \Delta f_c^2 + c}, \\ \text{CRB}_{\text{low}} &= \frac{3\bar{N}}{\pi^2((3\bar{N}^2 - 3\gamma^2)\Delta f_c^2 + \bar{N}^4 f_s^2 - \bar{N}^2 f_s^2)}, \end{aligned} \quad (14)$$

where $\Delta f_c = f_{c,2} - f_{c,1}$ denotes the frequency band apertures, $c = (N + \gamma)(\bar{N}^3 f_s^2 - \bar{N} f_s^2)\pi^2 + 3\bar{N}\gamma'' + 3\gamma\gamma'' - 3(\gamma')^2$ is a constant coefficient independent of Δf_c , and the definition of γ , γ' , and γ'' can be seen in Appendix C. **The derivation for CRB_{up} and CRB_{low} are presented in Appendix D.** Fig. 3 illustrates the square root of $C_{\Delta\tau}$, CRB_{up} , and CRB_{low} versus the delay separation $\Delta\tau$. As can be seen, CRB_{up} and CRB_{low} are tight enough to force $C_{\Delta\tau}$, which indicates that $C_{\Delta\tau}$ has similar properties with CRB_{up} and CRB_{low} . From (14), we conclude that CRB_{up} (CRB_{low}) decreases with the increase of Δf_c in the order $\mathcal{O}(1/(\Delta f_c)^2)$. Besides, due to that $\bar{N} > |\gamma|, \forall \Delta\tau$, the monotonicity between Δf_c and CRB_{up} (CRB_{low}) is not influenced by $\Delta\tau$.

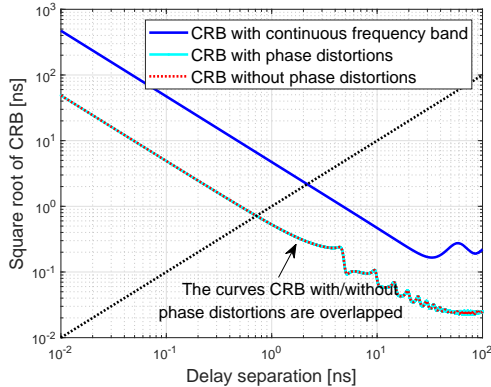


Fig. 4. An illustration of the square root CRB versus delay separation with $|\alpha_1| = 1, |\alpha_2| = 1$.

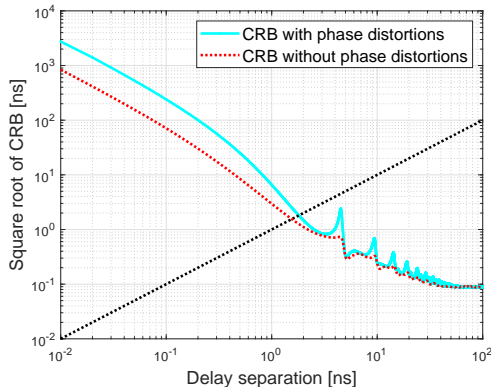


Fig. 5. An illustration of the square root CRB versus delay separation with $|\alpha_1| = 1, |\alpha_2| = 0.1$.

B. SRL for the Delay Resolution

To further reveal the effects of frequency band apertures and phase distortions on the fundamental limits of delay resolution and gain more insights, we introduce the delay SRL [19], which is defined as follows:

$$\begin{aligned} \text{SRL} &\triangleq \Delta\tau \\ \text{s.t. } \Delta\tau &= \sqrt{C_{\Delta\tau}}. \end{aligned} \quad (15)$$

The delay SRL is the delay separation that is equal to its own root squared CRB. In this definition, the delays can be exactly “resolved” when the standard deviation of the delay separation estimation is equal to the true separation. It is difficult to obtain a closed-form expression of delay SRL due to an intractable inverse operation corresponding to the high-dimensional matrix \mathbf{J}_η . Therefore, we perform a numerical computation and provide useful insights based on the numerical results.

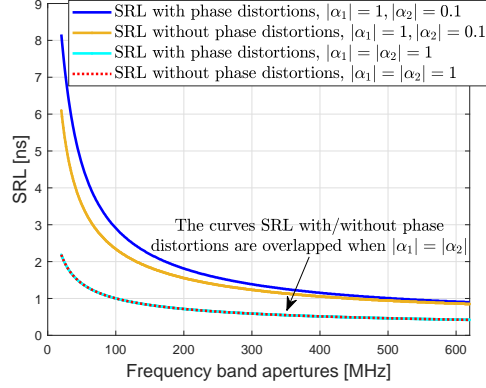


Fig. 6. An illustration of the SRL versus frequency band apertures.

C. Fundamental Limits Analysis Based on Numerical Results

In this subsection, we provide numerical results to study the effect of frequency band apertures and phase distortions on the fundamental limits of delay resolution. In the default setup, we consider that the measurements are collected at $M = 2$ subbands, with central frequencies $f_{c,1} = 1.8$ GHz and $f_{c,2} = 2.0$ GHz, subcarrier spacing $f_{s,1} = f_{s,2} = 78.125$ KHz, and subband bandwidth $B_1 = B_2 = 20$ MHz. Besides, $\varphi_m, \forall m$ and $\delta_m, \forall m$ are generated following a uniform distribution within $[0, 2\pi]$ and a Gaussian distribution $\mathcal{N}(0, \sigma_p^2)$, respectively. The signal-to-noise ratio (SNR) is set as 15 dB and the complex scalars are set as $\alpha_1 = 0.8 + 0.6j$ and $\alpha_2 = 0.6 + 0.8j$ with the unit amplitude.

Fig. 4 illustrates the square root of the CRB for the delay separation versus the delay separation in different scenarios, where the intersections of the CRB and the dotted black line give the delay SRL. We compare the CRB with phase distortions to two benchmarks: (i) An ideal scenario without phase distortions, i.e., $\varphi_m = 0, \forall m$ and $\delta_m = 0, \forall m$; (ii) An ideal scenario without phase distortions where only single contiguous frequency band is employed with 40 MHz equivalent bandwidth.

We have the following observations. First, the CRB based on two non-contiguous frequency bands is lower than the CRB based on a single contiguous frequency band with equivalent bandwidth, which leads to a higher delay resolution (lower delay SRL) brought by the frequency band apertures. Second, the curves of the CRB with/without phase distortions are completely overlapped. Furthermore, we plot Fig. 5, which illustrates the square root of CRB versus delay separation when $|\alpha_1| = 1, |\alpha_2| = 0.1$. The curves of the CRB with/without phase distortions are not overlapped anymore and the phase distortions slightly decline the performance of delay SRL. Therefore, a smaller difference between the amplitudes of the multipath can significantly suppress the phase distortion interference. In particular, when $|\alpha_1| = |\alpha_2|$, the phase distortions have no effect on the delay SRL. **To justify this observation, we first derive the EFIM of \mathbf{J}_η for θ given by**

$$[\mathbf{J}_\eta^{-1}]_{6 \times 6} \triangleq \mathbf{J}_e^{-1}(\theta) \stackrel{a}{=} (\mathbf{J}_\theta - \mathbf{B}_2 \mathbf{C}_2^{-1} \mathbf{B}_2^T)^{-1} \stackrel{b}{=} \mathbf{J}_\theta^{-1} + \mathbf{\Gamma}, \quad (16)$$

where $\theta = [\tau_1, \tau_2, \alpha_{R,1}, \alpha_{R,2}, \alpha_{I,1}, \alpha_{I,2}]^T$ denotes the vector consisting of the unknown parameters in η except for

phase distortions factors φ_m and δ_m , (16-a) follows the definition of EFIM, (16-b) follows the Woodbury identity [31], \mathbf{B}_2 and \mathbf{C}_2 are the entries of $\mathbf{J}_\eta \triangleq \begin{bmatrix} \mathbf{J}_\theta & \mathbf{B}_2 \\ \mathbf{B}_2^T & \mathbf{C}_2 \end{bmatrix}$, and

$$\boldsymbol{\Gamma} = \mathbf{J}_\theta^{-1} \mathbf{B}_2 (\mathbf{C}_2 - \mathbf{B}_2^T \mathbf{J}_\theta^{-1} \mathbf{B}_2)^{-1} \mathbf{B}_2^T \mathbf{J}_\theta^{-1}.$$

Based on the symbolic computation, we find that $\boldsymbol{\Gamma}$ has a special symmetrical structure as $\boldsymbol{\Gamma}(1,1) = \boldsymbol{\Gamma}(1,2) = \boldsymbol{\Gamma}(2,1) = \boldsymbol{\Gamma}(2,2)$. Then, $C_{\Delta\tau}$ derived from (10) can be further equivalently transformed as

$$\begin{aligned} C_{\Delta\tau} &= \mathbf{J}_\eta^{-1}(1,1) + \mathbf{J}_\eta^{-1}(2,2) - \mathbf{J}_\eta^{-1}(1,2) - \mathbf{J}_\eta^{-1}(2,1) \\ &\stackrel{c}{=} \mathbf{J}_\theta^{-1}(1,1) + \mathbf{J}_\theta^{-1}(2,2) - \mathbf{J}_\theta^{-1}(1,2) - \mathbf{J}_\theta^{-1}(2,1) \\ &\quad + \boldsymbol{\Gamma}(1,1) + \boldsymbol{\Gamma}(2,2) - \boldsymbol{\Gamma}(1,2) - \boldsymbol{\Gamma}(2,1) \\ &= \mathbf{J}_\theta^{-1}(1,1) + \mathbf{J}_\theta^{-1}(2,2) - \mathbf{J}_\theta^{-1}(1,2) - \mathbf{J}_\theta^{-1}(2,1), \end{aligned} \quad (17)$$

where (17-c) follows the equation (16). Finally, the CRB for the delay separation without φ_m and δ_m denoted as $\overline{C}_{\Delta\tau}$ is given by

$$\begin{aligned} \overline{C}_{\Delta\tau} &= \frac{\partial \Delta\tau^T}{\partial \theta} \mathbf{J}_\theta^{-1} \frac{\partial \Delta\tau}{\partial \theta} \\ &= \mathbf{J}_\theta^{-1}(1,1) + \mathbf{J}_\theta^{-1}(2,2) - \mathbf{J}_\theta^{-1}(1,2) - \mathbf{J}_\theta^{-1}(2,1). \end{aligned} \quad (18)$$

Therefore, from (17) and (18), we have $\overline{C}_{\Delta\tau} = C_{\Delta\tau}$, which justified the observations in Fig. 4, i.e., the curves SRL with/without phase distortions are overlapped.

In Fig. 6, we further investigate the effects of frequency band apertures on the delay SRL. We fix $f_{c,1}$ and change $f_{c,2}$ to generate different frequency band apertures. As can be seen, the SRL decreases with the increase of frequency band apertures, which is consistent with the monotonicity between $C_{\Delta\tau}$ and Δf_c concluded in Subsection III-A. Besides, when $|\alpha_1| = |\alpha_2|$, the SRL with/without phase distortions are always equal for different frequency band apertures. In contrast, when $|\alpha_1| \neq |\alpha_2|$, the SRL with/without phase distortions have a performance gap, that declines as the frequency band apertures increase.

Finally, we summarize the key messages learned from the analysis in this section.

- 1) **Monotonicity:** The CRB for delay separation $C_{\Delta\tau}$ decreases with the increase of frequency band apertures Δf_c in the order $\mathcal{O}(1/(\Delta f_c)^2)$ and the monotonicity is independent of delay separation $\Delta\tau$.
- 2) **Frequency band apertures gain:** (i) Under the equivalent total bandwidth, the multiband sensing system with non-contiguous frequency bands distribution reaps the extra frequency band apertures gain compared to that with a single contiguous frequency band distribution, which leads to a performance improvement of the delay resolution limit; (ii) The SRL decreases with the increase of frequency band apertures.
- 3) **Phase distortions interference:** (i) The phase distortions have relatively slight interference on delay SRL, which can be gradually eliminated by increasing the frequency band apertures; (ii) A smaller difference between the amplitudes of the multipath can suppress the phase distortion interference better. Particularly,

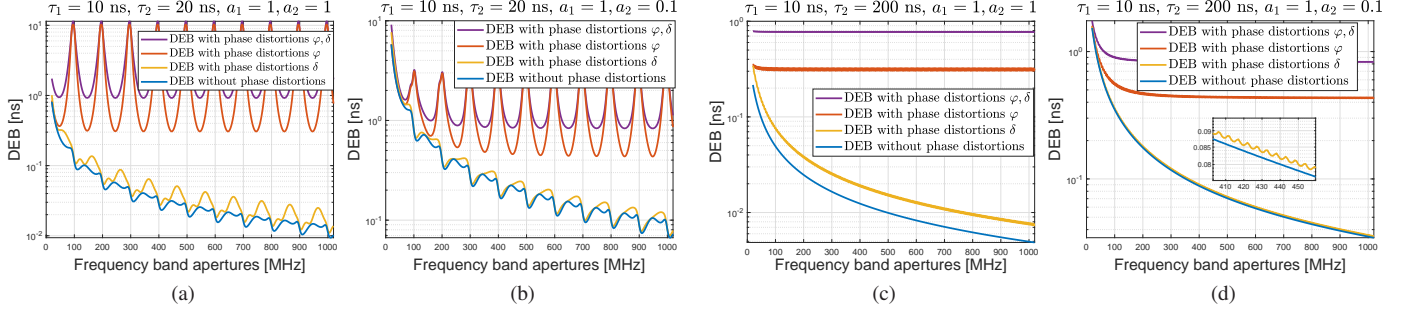


Fig. 7. An illustration of DEB versus frequency band apertures.

when $|\alpha_1| = |\alpha_2|$, the delay SRL is not affected by phase distortions at all.

IV. FUNDAMENTAL LIMITS OF DELAY ESTIMATION ERROR

A. CRB for the Delay Estimation Error

we characterize the fundamental limits of delay estimation error by a performance measure called delay error bound (DEB) as

$$\text{DEB} = \sqrt{\text{tr} \left\{ [\mathbf{J}_\eta^{-1}]_{K \times K} \right\}}, \quad (19)$$

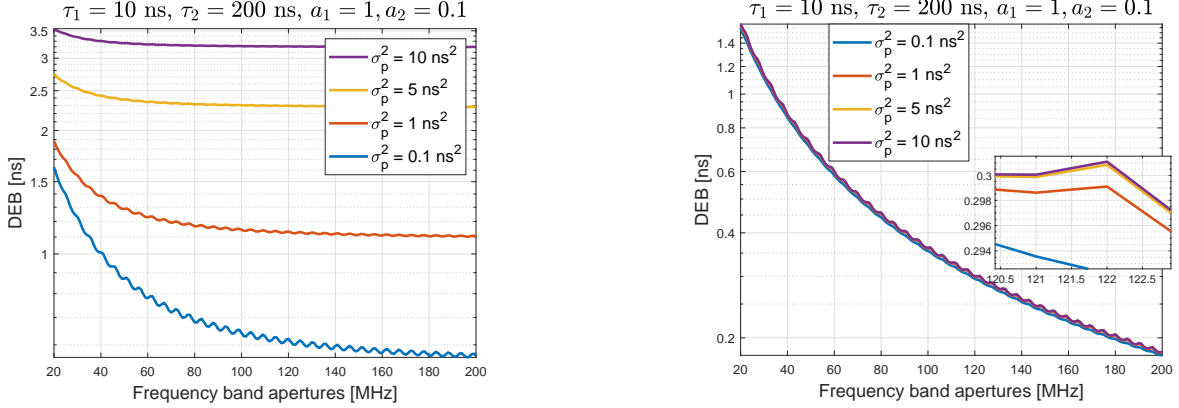
which is derived from the CRB. The notation $\text{tr} \left\{ [\mathbf{J}_\eta^{-1}]_{K \times K} \right\}$ denotes that we first get the inverse of the $(3K+2M-1) \times (3K+2M-1)$ matrix \mathbf{J}_η and then select the first $K \times K$ sub-matrix of \mathbf{J}_η^{-1} to take trace. Then, we analyze the effect of frequency band apertures and phase distortions on DEB based on numerical results. The parameters are set as that in Subsection III-C unless otherwise specified.

In Fig. 7, we consider four scenarios: (1) An ideal scenario without phase distortions; (2) A scenario with only random phase offset φ ; (3) A scenario with only receiver timing offset δ ; (4) A scenario with both phase distortions factors φ and δ . For each scenario, we consider different values of τ_2 and a_2 , as shown in Fig. 7a-Fig. 7d.

It is observed that both φ and δ lead to a larger DEB. Besides, in Fig. 7a, the DEB without phase distortions decreases as the frequency band aperture increases with a slight fluctuation. The fluctuation can be justified by the trigonometric term in (43) with regard to $f_{c,m}$, e.g., $\cos(2\pi f_{c,m} \Delta\tau + \phi_1)$, which is a periodic function with period $1/\Delta\tau$. In fact, we can observe that a harmonic component exists in all scenarios with period $1/\Delta\tau$ and the scenarios with φ have the most violent fluctuation of DEB. It reveals the difficulty of exploiting frequency band apertures gain for any algorithms in the presence of φ . However, as shown in Fig. 7b-Fig. 7d, if we increase $\Delta\tau$ and the difference between the amplitudes a_1 and a_2 , we will observe that the DEB decreases as the frequency band apertures increase with much weaker fluctuation, indicating that the frequency band apertures contribute to improving the delay estimation accuracy though in the presence of phase distortions.

In Fig. 8, we further investigate the effect of δ on DEB. As can be seen, the DEB increases with σ_p , which is reasonable since larger σ_p leads to little prior information of δ . Furthermore, in Fig. 8a, the value of σ_p dominates the behavior of DEB while in Fig. 8b, increasing the value of σ_p incurs only negligible performance loss. It is

because the prior information of δ is helpful to eliminate the ambiguity of signal model (4) in the presence of φ and δ . When in the absence of φ , the signal model (4) does not exist ambiguity anymore and thus the effect of prior information becomes negligible.



(a) DEB in the presence of phase distortion factors φ and δ .

(b) DEB in the presence of phase distortion factor δ .

Fig. 8. An illustration of DEB versus frequency band apertures for different σ_p^2 .

B. ZZB for the Delay Estimation Error

CRB is a local bound that may provide inaccurate predictions under conditions of low SNR or large frequency band apertures. Therefore, providing a global bound for the delay estimation error is necessary, which is capable of providing more accurate predictions of the performance of estimators over the full range of SNR and frequency band apertures.

In this subsection, we adopt a widely employed global bound ZZB as the fundamental limits of the multiband delay estimation problem. It is also a Bayesian bound that incorporates prior information of the unknown parameters and is not limited to unbiased estimates [23], [24], [25], [32]. We consider a scenario without phase distortions, where $K = 1$ with unknown parameters $\eta_1 = [\tau_1, \phi_1]^T$ for simplicity, since the calculation of ZZB for $K \geq 2$ is extremely difficult. The signal model in (4) can be reformulated as

$$y_{m,n} = |\alpha_1| e^{j\phi_1} e^{-j2\pi(f'_{c,m} + n f_{s,m})\tau_1} s_{m,n} + w_{m,n}. \quad (20)$$

The development of the ZZB links the delay estimation problem to a hypothesis testing problem that discriminates a signal at two possible delays. For a received signal at one of the two possible parameters value β or $\beta + \mathbf{e}$, where $\mathbf{e} = [e_{\tau_1}, e_{\phi_1}]^T$ denotes an offset, the hypothesis test denoted as \mathcal{P}_H is given by

$$\begin{aligned} \text{Decide } \mathcal{H}_0 : \eta_1 = \beta & \text{ if } \mathbf{u}^T \hat{\eta}_1 \leq \mathbf{u}^T \beta + \frac{h}{2}; \mathbf{y} \sim p_{\mathbf{y}|\eta_1}(\mathbf{y}|\beta), \\ \text{Decide } \mathcal{H}_1 : \eta_1 = \beta + \mathbf{e} & \text{ if } \mathbf{u}^T \hat{\eta}_1 > \mathbf{u}^T \beta + \frac{h}{2}; \mathbf{y} \sim p_{\mathbf{y}|\eta_1}(\mathbf{y}|\beta + \mathbf{e}), \end{aligned}$$

with prior probabilities $\Pr(\mathcal{H}_0) = P_0$ and $\Pr(\mathcal{H}_1) = P_1$. A more detailed discussion of the hypothesis test formulation may be found in [25]. Note that \mathbf{u} can be any 2-dimensional vector and $\hat{\eta}_1$ denotes an estimator of η_1 . Let

$P_{\min}(\boldsymbol{\beta}, \boldsymbol{\beta} + \mathbf{e})$ denotes minimal probability of error achieved by the optimum detection scheme in making the above decision. Then, the ZZB for the quadratic form of the MSE matrix is given by [24]

$$\begin{aligned} \mathbf{u}^T \boldsymbol{\Phi} \mathbf{u} \geq & \frac{1}{2} \int_0^\infty \mathcal{V} \left\{ \max_{\mathbf{e}: \mathbf{u}^T \mathbf{e} = h} \int_{\Theta} [p_{\boldsymbol{\eta}_1}(\boldsymbol{\beta}) + p_{\boldsymbol{\eta}_1}(\boldsymbol{\beta} + \mathbf{e})] \right. \\ & \left. \times P_{\min}(\boldsymbol{\beta}, \boldsymbol{\beta} + \mathbf{e}) d\boldsymbol{\beta} \right\} h dh, \end{aligned} \quad (21)$$

where $\boldsymbol{\Phi} \triangleq \mathbb{E}_{\mathbf{y}, \boldsymbol{\eta}_1} \{(\hat{\boldsymbol{\eta}}_1 - \boldsymbol{\eta}_1)(\hat{\boldsymbol{\eta}}_1 - \boldsymbol{\eta}_1)^H\}$ denotes the MSE matrix, Θ denotes the region in which $\boldsymbol{\eta}_1$ is defined, $\mathcal{V}\{\cdot\}$ denotes the valley-filling function [25], and $p_{\boldsymbol{\eta}_1}(\cdot)$ denotes the prior distribution of the unknown parameters vector $\boldsymbol{\eta}_1$. Given the prior distribution, the ZZB is evaluated involving an integral of a product for the known prior distribution and the minimum detection error probability. Therefore, to compute the ZZB, the minimum detection error probability is the major unknown component needed to calculate. In the subsequent content, we will first evaluate $P_{\min}(\boldsymbol{\beta}, \boldsymbol{\beta} + \mathbf{e})$ by calculating the error probability of the optimum log-likelihood ratio (LLR) test for \mathcal{P}_H , and then substitute the expression of $P_{\min}(\boldsymbol{\beta}, \boldsymbol{\beta} + \mathbf{e})$ into (21) to compute the ZZB.

Consider a pair of equally likely hypotheses in \mathcal{P}_H , where the prior probability $\Pr(\mathcal{H}_0) = \Pr(\mathcal{H}_1) = 1/2$. Then the minimum probability of error $P_{\min}(\boldsymbol{\beta}, \boldsymbol{\beta} + \mathbf{e})$ can be obtained from the LLR test [28] as

$$P_{\min}(\boldsymbol{\beta}, \boldsymbol{\beta} + \mathbf{e}) = \frac{1}{2} \Pr(\zeta < 0 | H_0) + \frac{1}{2} \Pr(\zeta > 0 | H_1),$$

where ζ is the LLR for the hypothesis test given by

$$\zeta = \ln p_{\mathbf{y}|\boldsymbol{\eta}_1}(\mathbf{y} | \boldsymbol{\beta}) - \ln p_{\mathbf{y}|\boldsymbol{\eta}_1}(\mathbf{y} | \boldsymbol{\beta} + \mathbf{e}).$$

Let $\mathbf{y}_i \triangleq \mathbf{y} | \mathcal{H}_i$, $\zeta_i \triangleq \zeta | \mathcal{H}_i$, $i = 0, 1$, then $\zeta_i \propto \text{Re}\{(\mathbf{u}_0 - \mathbf{u}_1)^H \mathbf{y}_i\}$, $\forall i$, where

$$\mathbf{u}_0 = [u_0(1, -\frac{N_m - 1}{2}), \dots, u_0(M, \frac{N_m - 1}{2})]^T,$$

whose (m, n) -th element is given by

$$u_0(m, n) = |\alpha_1| e^{j\beta\phi_1} e^{-j2\pi(f'_{c,m} + n f_{s,m})\beta\tau_1}, \forall m, n.$$

Similarly, \mathbf{u}_1 is a vector whose (m, n) -th element is

$$u_1(m, n) = |\alpha_1| e^{j(\beta\phi_1 + e_{\phi_1})} e^{-j2\pi(f'_{c,m} + n f_{s,m})(\beta\tau_1 + e_{\tau_1})}.$$

Note that the LLR ζ is a linear combination of Gaussian variables, we can get the expectation and variance of ζ_0 and ζ_1 as

$$\begin{aligned} \mathbb{E}[\zeta_0] &= -\mathbb{E}[\zeta_1] \propto |\alpha_1|^2 (N - \sum_{m,n} \cos(-2\pi f_{m,n} e_{\tau_1} + e_{\phi_1})), \\ \mathbb{D}[\zeta_0] &= \mathbb{D}[\zeta_1] \propto \sigma_{ns}^2 |\alpha_1|^2 (N - \sum_{m,n} \cos(-2\pi f_{m,n} e_{\tau_1} + e_{\phi_1})). \end{aligned}$$

As can be seen, $P_{\min}(\boldsymbol{\beta}, \boldsymbol{\beta} + \mathbf{e})$ is only a function of the offset \mathbf{e} and thus can be denoted by $P_{\min}(\mathbf{e})$, which is

given by

$$\begin{aligned} P_{\min}(\mathbf{e}) &= Q\left(\frac{\mathbb{E}[\zeta_0]}{\sqrt{\mathbb{D}[\zeta_0]}}\right) \\ &= Q\left(\frac{|\alpha_1|}{\sqrt{\sigma_{ns}^2}} \sqrt{N - \sum_{m,n} \cos(-2\pi f_{m,n} e_{\tau_1} + e_{\phi_1})}\right), \end{aligned}$$

where $Q\{\cdot\}$ denotes the tail distribution function of the standard normal distribution, i.e., $Q(x) = \frac{1}{\sqrt{2\pi}} \int_x^\infty e^{-\frac{v^2}{2}} dv$. Assume that the unknown parameters τ_1 and ϕ_1 are independent random variables, which are uniformly distributed in $[0, D]$ ns and $[0, 2\pi]$, respectively. Then, substituting $\mathbf{u} = [1, 0]^T$ in (21), the ZZB for the delay estimation error is given by

$$\begin{aligned} \text{ZZB}_{\tau_1} &= \mathbf{u}^T \Phi \mathbf{u} \Big|_{\mathbf{u}=[1,0]^T} = \Phi(1, 1) \\ &\geq \frac{1}{2\pi D} \int_0^D e_{\tau_1} \mathcal{V} \left\{ (D - e_{\tau_1}) \max_{e_{\phi_1}} (2\pi - e_{\phi_1}) P_{\min}(\mathbf{e}) \right\} de_{\tau_1}. \end{aligned}$$

There is no closed-form expression of ZZB_{τ_1} , so we perform a numerical computation to obtain its value. We compare the derived ZZB with MSEs of the MAP delay estimator and the expected CRB (ECRB) [33]. **The MAP estimation results are obtained based on a 2-dimensional exhausted search for variables τ_1 and ϕ_1 . The root MSE (RMSE) of MAP estimates is then calculated over 200 Monte Carlo trials.** The ECRB is obtained by taking the expectation of the conditional CRB with respect to the random but unknown parameters $\boldsymbol{\eta}_1$, namely

$$\text{ECRB} = \mathbb{E}_{\boldsymbol{\eta}_1} [\text{CRB}(\boldsymbol{\eta}_1)]. \quad (22)$$

In the default setup, we consider two subbands with subcarrier spacing $f_{s,1} = f_{s,2} = 78.125$ KHz and bandwidth $B_1 = B_2 = B$, where $B = 20$ MHz. SNR is 10 dB and $D = 10$. From Fig. 9 where the frequency band aperture $\Delta f_c = 0.5$ GHz, the curve of ZZB versus SNR can be divided into three regions. In the low SNR region, the ZZB provides a tighter bound than ECRB. Besides, the ZZB reaches a plateau equal to the standard deviation of the prior distribution of τ_1 , that can be computed as $\sqrt{D^2/12}$, due to that the sensing performance is mainly dominated by prior information when SNR is low. For the high SNR region, the ZZB merges with the ECRB and MAP. Besides, the ZZB predicts the MAP threshold behavior and a transition region is observed between the low and high SNR regions.

Fig. 10 displays the ZZB, ECRB, and MSEs of the MAP estimates as a function of frequency band apertures. As can be seen, the ZZB provides a bound at least as tight or tighter than the ECRB in most frequency band apertures regions. Besides, the MAP threshold behavior emerges as the frequency band apertures increase, i.e., the RMSE of MAP estimator decreases first and then rapidly increases with the increase of frequency band apertures. It can be justified that though larger frequency band apertures result in a sharper mainlobe of the likelihood function, which reveals a potential sensing performance gain, it also leads to a multimodal likelihood function that has more sidelobes. The MAP estimator will be affected by ambiguities created by the sidelobes. Moreover, similar to the observations in Fig. 9, the ZZB again predicts the MAP threshold behavior while the ECRB does not track the MAP threshold behavior. It is reasonable since the ECRB is a local bound whereas the ZZB is a global bound. Inspired

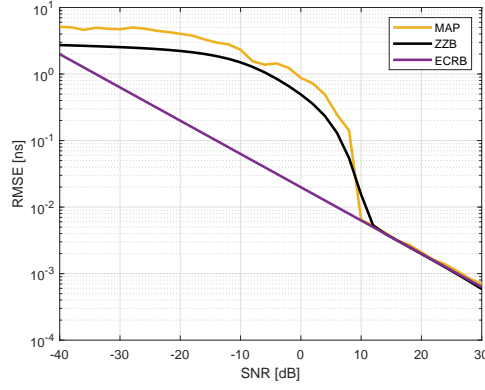


Fig. 9. An illustration of ZZB with MAP and ECRB comparison versus SNR.

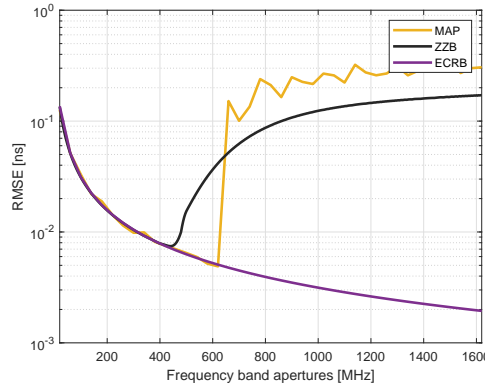


Fig. 10. An illustration of ZZB with MAP and ECRB comparison versus frequency band apertures.

by these observations, the frequency band apertures should be restricted to a limited range in practical multiband sensing systems, in order to avoid causing a performance loss and fully exploit the frequency band apertures gain.

Fig. 11 and Fig. 12 illustrate the effect of SNR and bandwidths on the ZZB, respectively. It can be seen that the ZZB decreases with the increase of SNR or bandwidth. Besides, the threshold behavior emerges in a larger frequency band aperture as the SNR or bandwidth increases, due to that the ambiguities caused by sidelobes are significantly reduced.

Though the above results are obtained based on a single target signal model, the observations can also be observed based on a multiple targets signal model with phase distortions considered. Due to the difficulty of computing the ZZB associated to a multi-parameter estimation problem, we plot Fig. 13 to just illustrate the RMSE of the MAP estimator as a function of frequency band apertures based on the multiple targets signal model (4), where the parameters are set as that in Subsection III-C. As can be seen, the MAP threshold behavior appears as expected.

Finally, we summarize the key messages learned from the analysis in this section.

- 1) **Monotonicity:** (i) The DEB without phase distortions factors φ decreases as the frequency band aperture increases with a slight fluctuation; (ii) Generally, both the DEB with/without phase distortions fluctuate as a

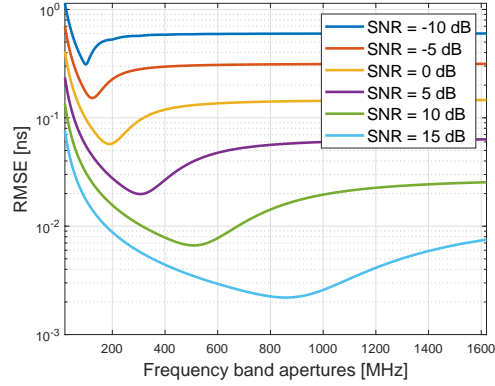


Fig. 11. An illustration of ZZB versus frequency band apertures for different SNRs.

function of frequency band apertures due to the existence of trigonometric terms whose period is $1/\Delta\tau$.

- 2) **Interference of random phase offset φ :** The existence of φ leads to a larger DEB with violent fluctuation and thus makes it difficult to exploit the frequency band apertures gain for any methods. However, when the targets are distinguishable with significantly different time delay and amplitudes, the DEB decreases as the frequency band apertures increase smoothly, which unveils a delay estimation performance gain brought by the frequency band apertures even though in the presence of phase distortions.
- 3) **Interference of receiver timing offset δ :** The existence of δ leads to a larger DEB, but this negative effect can be suppressed by increasing the prior information of δ . Specifically, for the signal model (4) in the presence of φ and δ , the DEB significantly decreases with σ_p since the prior information eliminates the signal model ambiguity efficiently. For the signal model (4) in the absence of φ , the effect of prior information becomes relatively negligible since the signal model does not exist ambiguity anymore.
- 4) **ZZB behavior:** (i) The ZZB provides a tighter bound than the ECRB in all frequency band apertures regions and SNR regions; (ii) The ZZB predicts the MAP threshold behavior, which emerges as the frequency band apertures increase or the SNR decreases. Hence, the subbands need to be selected carefully and the frequency band apertures should be restricted to a limited range in practical multiband sensing systems, in order to fully exploit the frequency band apertures gain; (iii) Increasing the the SNR or bandwidth can delay the occurrence of the threshold behavior as frequency band apertures increase.

V. OPTIMIZATION OF MULTIBAND SENSING SYSTEMS

The fundamental limits analysis discussed above implies that it is possible to improve the sensing performance of the multiband sensing system by system parameter optimization, e.g., increasing the frequency band apertures of the subbands may improve the system's sensing resolution.

Therefore, in this section, we present the optimization of multiband sensing systems with the objective of minimizing the fundamental limit, delay SRL under a few practical constraints. The reason we adopt the delay SRL as the objective function is that the delay SRL is less affected by the phase distortions than DEB and requires

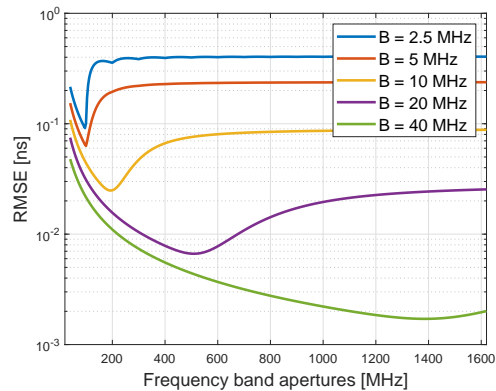


Fig. 12. An illustration of ZZB versus frequency band apertures for different bandwidths.

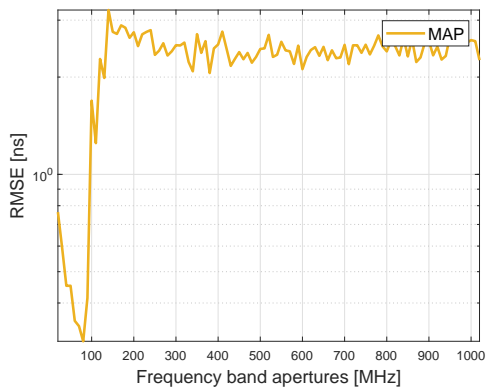


Fig. 13. An illustration of MAP estimator versus frequency band aperture based on a multiple targets signal model.

less information to calculate (e.g., only estimated mean amplitude information is required to calculate the SRL in practical scenarios, as will be explained later). In fact, the optimized results with the objective of minimizing the delay SRL is also effective to decrease the DEB, as will be shown in the simulations.

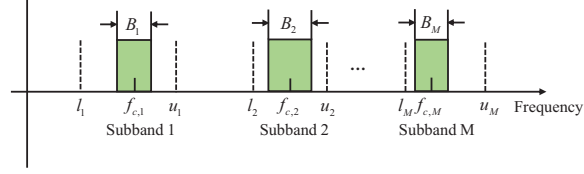


Fig. 14. An illustration of the frequency distribution of the multiband sensing systems with constraints.

A. Problem Formulation

At the transmitter of the multiband sensing systems, we aim to optimize the system parameters for minimizing the delay SRL subject to a few practical constraints. The optimization problem can be formulated as

$$\mathcal{P} : \min_{\xi, \Delta\tau} \Delta\tau(\xi)$$

$$\text{s.t. } \sqrt{C_{\Delta\tau}(\Delta\tau, \xi)} = \Delta\tau, \quad (23)$$

$$l_m \leq f_{c,m} - \frac{B_m}{2}, \forall m, \quad (24)$$

$$f_{c,m} + \frac{B_m}{2} \leq u_m, \forall m, \quad (25)$$

$$f_{c,m} + \frac{B_m}{2} \leq f_{c,m+1} - \frac{B_{m+1}}{2}, m=1, \dots, M-1, \quad (26)$$

$$\sum_{m=1}^M B_m \leq W, \quad (27)$$

where $\xi = [f_{c,1}, \dots, f_{c,M}, N_1, \dots, N_M]^T$ denotes the vector consisting of system parameters needed to be optimized. Choosing the carrier frequency $f_{c,m}$ and subcarrier number N_m of each subband as the optimization variables is reasonable, since in current communication standards (e.g., IEEE 802.11bf standard [34]), the subcarrier spacing $f_{s,m}$ is always fixed and only $f_{c,m}$ and N_m are able to be optimized. Note that $B_m = N_m f_{s,m}$ denotes the bandwidth of the m -th subband, the constraint (23) is the definition of SRL, and (27) is the total bandwidth constraint, where W denotes the maximum available bandwidth for sensing over all subbands. The constraints (24) and (25) are formulated to limit the frequency of each subband in a given interval since only a few non-contiguous subbands are available for sensing with limited bandwidths in practical communication standards, where l_m and u_m denote the lower bound and upper bound of the frequency for the m -th subband, respectively. The constraints (26) are formulated to ensure that different subbands are not overlapped after optimization. The above mentioned parameters have been shown in Fig. 14 for clarity.

Note that the definition of delay SRL only involves two paths. However, the proposed optimization scheme can still be applied to a practical multipath environment with more than two paths and the effectiveness has been validated by simulation results. Specifically, we can solve problem \mathcal{P} with the SRL objective calculated using the estimated mean amplitude $\tilde{\alpha}_1 = \tilde{\alpha}_2 = \frac{1}{\hat{K}} \sum_{k=1}^{\hat{K}} |\hat{\alpha}_k|$, to get a solution ξ for the system parameter, where the number of paths \hat{K} and the amplitude for each path $\hat{\alpha}_k$ can be estimated in the previous time slot using a multiband delay estimation algorithm, e.g., [35].

B. Proposed Optimization Algorithm

\mathcal{P} is a mixed-integer nonlinear programming (MINLP) problem, which involves the integer optimization variables $N_m, \forall m$ with the form of summation terms in the expression of $C_{\Delta\tau}(\Delta\tau, \boldsymbol{\xi})$ (As can be seen in (41)). Finding an optimal solution of a MINLP problem is intractable because it is generally non-deterministic Polynomial-time hard (NP-hard). Furthermore, the non-convex equality constraint in \mathcal{P} makes it more difficult to solve.

To handle these issues, some optimization techniques have been proposed to find a sub-optimal solution to the original problem, such as convex relaxation techniques [36], [37], metaheuristic techniques [38], [39], and so on. However, most methods can only find a local or approximate solution with high computational complexity. To reduce complexity and make the problem tractable, we consider a widely employed integer relaxation techniques [40], [41]. Specifically, we first relax the integer variable N_m to a real variable and calculate $C_{\Delta\tau}(\Delta\tau, \boldsymbol{\xi})$ using the compact form of FIM in (43), which transforms the summation terms into a trigonometric product form. Then, we adopt the AO algorithm to find a stationary point of \mathcal{P} by alternatively optimizing the variables of delay separation $\Delta\tau$ and system parameters $\boldsymbol{\xi}$. Finally, we round down the results of N_m to obtain approximate integer solutions. The approximation error caused by rounding down operation is acceptable, since it is relatively negligible as compare to the absolute value of N_m , which is always large in an OFDM system.

For given $\boldsymbol{\xi}$, the subproblem is to find a global minimum solution that satisfies the equality (23):

$$\begin{aligned} \mathcal{P}_1 : \quad & \min_{\Delta\tau} \quad \Delta\tau \\ & \text{s.t.} \quad \sqrt{C_{\Delta\tau}(\Delta\tau, \boldsymbol{\xi})} = \Delta\tau. \end{aligned} \quad (28)$$

The solution can be easily found by one-dimensional search of $\Delta\tau$ with acceptable computational complexity. Then, for given $\Delta\tau$, the subproblem transformed from \mathcal{P} is given by

$$\begin{aligned} \mathcal{P}_2 : \quad & \min_{\boldsymbol{\xi}} \quad C_{\Delta\tau}(\boldsymbol{\xi}) \\ & \text{s.t.} \quad (24) - (27). \end{aligned} \quad (29)$$

The subproblem \mathcal{P}_2 is a non-convex optimization problem with linear inequality constraints and complicated non-convex objective function $C_{\Delta\tau}(\boldsymbol{\xi})$. Thus we adopt the SCA algorithm [42], [43] to find its stationary solution, which iteratively updates $\boldsymbol{\xi}$ by solving a convex surrogate problem obtained by replacing $C_{\Delta\tau}(\boldsymbol{\xi})$ with a convex surrogate function. Specifically, the SCA algorithm contains three steps at each iteration as elaborated below.

Step 1: At the t -th iteration, by applying the first-order Taylor expansion for $C_{\Delta\tau}(\boldsymbol{\xi})$, the surrogate function is given by

$$\bar{f}^t(\boldsymbol{\xi}) = f(\boldsymbol{\xi}^t) + (\mathbf{g}_{\boldsymbol{\xi}}^t)^T (\boldsymbol{\xi} - \boldsymbol{\xi}^t) + \omega \|\boldsymbol{\xi} - \boldsymbol{\xi}^t\|^2, \quad (30)$$

where $f(\boldsymbol{\xi}^t) = C_{\Delta\tau}(\boldsymbol{\xi}^t)$, $\omega > 0$ is a constant, and $\mathbf{g}_{\boldsymbol{\xi}}^t = \partial_{\boldsymbol{\xi}} C_{\Delta\tau}(\boldsymbol{\xi}^t)$ denotes the gradients, of which the i -th

element is given by

$$\begin{aligned}
g_{\xi_i}^t &= \frac{\partial C_{\Delta\tau}(\boldsymbol{\xi}^t)}{\partial \xi_i} \\
&= \frac{\partial(\mathbf{C}_\eta^t(1,1) + \mathbf{C}_\eta^t(2,2) - \mathbf{C}_\eta^t(1,2) - \mathbf{C}_\eta^t(2,1))}{\partial \xi_i} \\
&= \mathbf{F}_i(1,1) + \mathbf{F}_i(2,2) - \mathbf{F}_i(1,2) - \mathbf{F}_i(2,1),
\end{aligned} \tag{31}$$

where $\mathbf{F}_i \triangleq -\mathbf{J}_\eta^{-1} \frac{\partial \mathbf{J}_\eta}{\partial \xi_i} \mathbf{J}_\eta^{-1}$.

Step 2: In this step, the optimal solution $\bar{\boldsymbol{\xi}}^t$ of the following problem is obtained:

$$\begin{aligned}
\mathcal{P}'_2 : \quad & \min_{\boldsymbol{\xi}} \quad \bar{f}^t(\boldsymbol{\xi}) \\
& \text{s.t.} \quad (24) - (27),
\end{aligned} \tag{32}$$

which is a convex approximation of \mathcal{P}_2 . Then, the convex optimization problem \mathcal{P}'_2 can be efficiently solved by off-the-shelf solvers, e.g. the classical CVX solver.

Step 3: After obtaining $\bar{\boldsymbol{\xi}}^t$, $\boldsymbol{\xi}^t$ is updated according to

$$\boldsymbol{\xi}^{t+1} = (1 - \sigma^t) \boldsymbol{\xi}^t + \sigma^t \bar{\boldsymbol{\xi}}^t, \tag{33}$$

where σ^t is the step size determined by the Armijo rule [44].

The proposed optimization algorithms are presented in Algorithm 1. Note that to improve the probability of finding the global optimum, we may repeatedly perform Algorithm 1 with random initializations and finally find the best solution. Finally, we prove the convergence of the Algorithm 1.

Lemma 1. *Let $\{\boldsymbol{\xi}^i, \Delta\tau^i\}_{i=1}^\infty$ denote the sequence of iterates generated by Algorithm 1. Then, $\{\Delta\tau^i\}_{i=1}^\infty$ is a non-increasing sequence.*

Proof: See Appendix E.

From Lemma 1, the sequence $\{\Delta\tau^i\}_{i=1}^\infty$ must converge to a limit $\Delta\tau^* > 0$, i.e.,

$$\lim_{i \rightarrow \infty} \Delta\tau^i = \Delta\tau^*. \tag{34}$$

In the following theorem, we further prove that the sequence $\{\boldsymbol{\xi}^i, \Delta\tau^i\}_{i=1}^\infty$ converges to a stationary point that satisfies KKT conditions of the following equivalent problem of \mathcal{P} :

$$\begin{aligned}
\mathcal{P}_e : \quad & \min_{\boldsymbol{\xi}, \Delta\tau} \quad C_{\Delta\tau}(\Delta\tau, \boldsymbol{\xi}) \\
& \text{s.t.} \quad h(\boldsymbol{\xi}, \Delta\tau) = 0, \\
& \quad \quad g_j(\boldsymbol{\xi}) \leq 0, j = 1, \dots, J,
\end{aligned}$$

where $h(\boldsymbol{\xi}, \Delta\tau) \triangleq \sqrt{C_{\Delta\tau}(\Delta\tau, \boldsymbol{\xi})} - \Delta\tau$ and $g_j(\boldsymbol{\xi}), \forall j$ represents all inequality constraints in original problem \mathcal{P} .

Theorem 1. *(Convergence of Algorithm 1): Starting from a feasible initial point $\{\boldsymbol{\xi}^0, \Delta\tau^0\}$, then sequence*

Algorithm 1 The multiband sensing system parameters optimization algorithm

Input: $f_{s,m}, l_m, u_m, \forall m, \alpha, \sigma_{n_s}^2, W$, maximum iteration number I_{AO}, I_{SCA} , threshold ϵ .

Output: $f_{c,m}^*, N_m^*, \forall m$.

```

1: Initialize  $f_{c,m}, N_m, \forall m$ .
2: for  $i = 1, \dots, I_{AO}$  do
3:   Given  $\xi^{i-1}$ , solve the problem  $\mathcal{P}_1$ .
4:   for  $t = 1, \dots, I_{SCA}$  do
5:     Given  $\Delta\tau^i$ , construct surrogate functions based on (30) and (31).
6:     Find the optimal solution  $\bar{\xi}^t$  for the problem  $\mathcal{P}'_2$ .
7:     Update the variables  $\xi^{t+1}$  based on (33).
8:     if  $\|\xi^{t+1} - \xi^t\| \leq \epsilon$  then
9:       break
10:    end if
11:  end for
12:   $\xi^i = \xi^t$ 
13: end for

```

$\{\xi^i, \Delta\tau^i\}_{i=1}^{\infty}$ generated by Algorithm 1 has a limiting point which is a KKT point of \mathcal{P}_e .

Proof: See Appendix F.

C. Simulation Results

In this subsection, we provide numerical results to validate the effectiveness of our proposed algorithms and give useful insights. The default system parameters configurations are set as follows unless otherwise specified: We consider that the measurements are collected at $M = 2$ subbands with subcarrier spacing $f_{s,1} = f_{s,2} = 78.125$ KHz. The SNR is set as 10 dB and $K = 2$ with complex scalars set as $\alpha_1 = 0.8 + 0.6j$ and $\alpha_2 = 0.6 + 0.8j$. The overall bandwidth constraint W is 40 MHz, and $l_1, u_1, l_2, u_2 = 2.4, 2.5, 2.7, 2.9$ GHz with an increasing order, respectively. Note that we deliberately restrict our attention to this simple case with equal subcarrier spacing at two subbands to gain insights, although our formulated problem and proposed optimization algorithms are applicable for more practical scenarios.

We first illustrate the convergence behavior of the proposed Algorithm 1. In Fig. 15, we plot the delay SRL versus the number of AO iterations. As can be seen, Algorithm 1 can converge within 5 iterations rapidly.

In Fig. 16a, we investigate the optimized results of delay SRL versus the SNR. In particular, we consider two heuristic baselines: (i) Baseline 1: Setting $f_{c,1} = \frac{l_1+u_1}{2}$, $f_{c,2} = \frac{l_2+u_2}{2}$, and $B_1 = B_2 = W/2$; (ii) Baseline 2: Setting $f_{c,1} = l_1 + B_1/2$, $f_{c,2} = u_2 - B_2/2$, and $B_1 = B_2 = W/2$. To verify the effectiveness of the proposed optimization scheme using the estimated mean amplitude information (imperfect), we compare the performance of the proposed scheme with estimated and perfect amplitude information (perfect) as well as the baselines in Fig. 16a. It is observed that: (1) The proposed schemes with imperfect and perfect information achieve similar performance, indicating that the approximation errors of α_k 's have little impact on the final optimization results; (2) The delay SRL decreases with the increase of SNR for all schemes; (3) The optimized scheme reaps a large performance

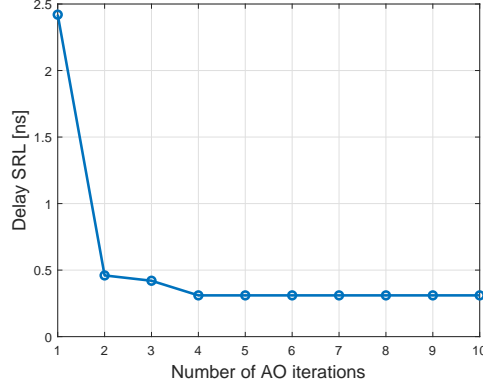


Fig. 15. Convergence behavior of Algorithm 1.

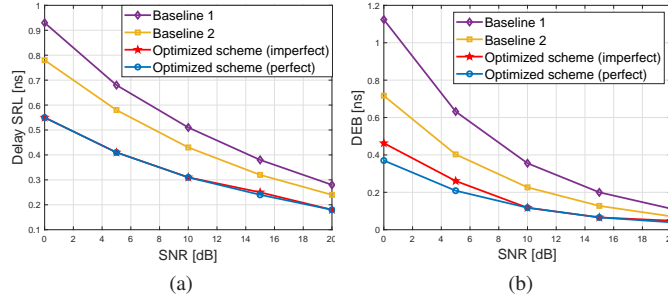


Fig. 16. An illustration of the SRL and DEB versus SNR.

gain over the baselines in the low and median SNR region; (4) Allocating the spectrum resource uniformly among subbands (i.e., $B_m = W/M, \forall m$) is not the optimal scheme.

Fig. 16b investigates DEB as a function of SNR based on the optimized variables, which are obtained from the output of Algorithm 1. As can be seen, the optimization scheme can significantly decrease the DEB compared to the baselines, though the objective of the optimization problem is to minimize the delay SRL instead of DEB.

Fig. 17 shows the SRL as a function of subcarrier spacing for different number of subbands, where the bandwidth constraint $W = 60$ MHz. The constrains (24) and (25) are set as in Table II. It can be seen that the SRL increases as the subcarrier spacing. Moreover, from the frequency band distribution after optimization illustrated in Fig. 18 and the optimal SRL shown in Fig 17, we observe that:

- 1) The best delay SRL is obtained when the gap between the lowest frequency point and the highest frequency point takes the maximum value, i.e., $f_{c,1} = l_1 + \frac{B_1}{2}$ and $f_{c,M} = u_M - \frac{B_M}{2}$. In fact, the gap is approximately equivalent to the largest frequency band apertures, $f_{c,M} - f_{c,1}$. The delay SRL decreases with the increase of the largest frequency band apertures, which is consistent with the observations in Fig. 6.
- 2) From the comparison of the cases $M = 2$ and $M = 3$, we observe that interpolating a new subband between the existing two subbands can significantly improve the resolution performance.

TABLE II
THE SETTING OF CONSTRAINTS IN \mathcal{P}_2 .

	$[l_1, u_1]$ GHz	$[l_2, u_2]$ GHz	$[l_3, u_3]$ GHz	$[l_4, u_4]$ GHz
$M = 2$	[2.4, 2.5]	[3.1, 3.2]	\	\
$M = 3$	[2.4, 2.5]	[2.7, 2.9]	[3.1, 3.2]	\
$M = 4$ (a)	[2.4, 3.2]	[2.4, 3.2]	[2.4, 3.2]	[2.4, 3.2]
$M = 4$ (b)	[2.4, 2.5]	[2.7, 2.9]	[3.1, 3.2]	[3.2, 3.3]

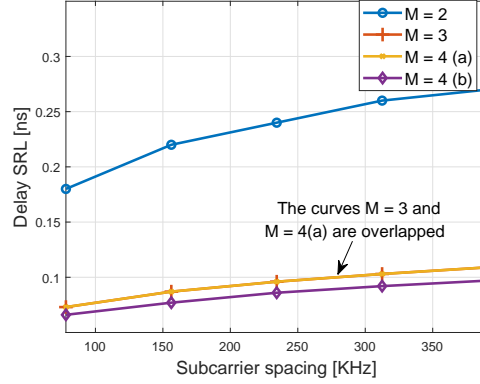


Fig. 17. An illustration of SRL versus subcarrier spacing.

- 3) For the cases when $M \geq 3$, the optimal spectrum allocation scheme is similar, which divides the frequency band into three non-contiguous subbands. Particularly, the middle subband is exactly at the central of the subbands on both sides when it also satisfies the constraints that lies in the feasible frequency intervals.

VI. CONCLUSION

In this paper, we studied the fundamental limits and optimization of the multiband sensing systems. We derived a closed-form expression of CRB for the delay separation and a corresponding theoretical analysis is provided. We derived the SRL for the delay resolution and studied the effect of frequency band apertures and phase distortions on the SRL based on numerical results. We also derived performance bounds CRB and ZZB for the delay estimation errors and give a comprehensive performance analysis. Finally, we formulated a system parameters optimization problem in the multiband sensing systems. An efficient algorithm has been proposed to solve the non-convex optimization problem and useful insights are provided based on numerical simulations.

APPENDIX

A. Proof of Parameter Identifiability in (4)

We consider two cases for the proof: (i) $\delta_m = 0, \forall m$; (ii) $\delta_m \neq 0, \forall m$.

(i) $\delta_m = 0, \forall m$. In this case, the signal model (4) can be rewritten as

$$y_{m,n} = \sum_{k=1}^K \alpha'_k e^{-j2\pi f'_{c,m} \tau_k} e^{-j2\pi n f_{s,m} \tau_k} e^{j\varphi'_m} s_{m,n} + w_{m,n}. \quad (35)$$

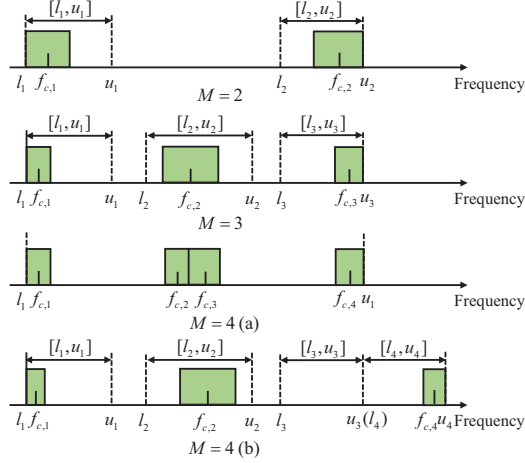


Fig. 18. An illustration of the optimal frequency band distribution.

Proving the parameter identifiability is equivalent to prove that the “identifiability equations” of (35) have a unique solution, which is given by

$$\sum_{k=1}^K \check{\alpha}'_k e^{-j2\pi f'_{c,m} \check{\tau}_k} e^{-j2\pi n f_{s,m} \check{\tau}_k} e^{j\check{\varphi}'_m} = \sum_{k=1}^K \alpha'_k e^{-j2\pi f'_{c,m} \tau_k} e^{-j2\pi n f_{s,m} \tau_k} e^{j\varphi'_m}, \quad (36)$$

$m = 1, \dots, M, n = 1, \dots, N_m.$

We denote the unique solution of equality (36) as: $\check{\alpha}'_k = \alpha'_k$, $\check{\tau}_k = \tau_k$, $\check{\varphi}'_m = \varphi'_m$, $k = 1, \dots, K$, $m = 2, \dots, M$. We first prove that $\check{\alpha}'_k = \alpha'_k$, $\check{\tau}_k = \tau_k$ is the unique solution of (36). Then, we prove that $\check{\varphi}'_m = \varphi'_m$ is also the unique solution of (36) to complete the proof.

When $m = 1$, the “identifiability equations” are given by

$$\sum_{k=1}^K \check{\alpha}'_k e^{-j2\pi n f_{s,1} \check{\tau}_k} = \sum_{k=1}^K \alpha'_k e^{-j2\pi n f_{s,1} \tau_k}, \quad n = 1, \dots, N_1,$$

which can be equivalently transformed to a linear form

$$\check{\mathbf{A}}\check{\boldsymbol{\beta}} = \mathbf{A}\boldsymbol{\beta}, \quad (37)$$

where

$$\mathbf{A} = \begin{bmatrix} e^{-j2\pi(-\frac{N_1-1}{2})f_{s,1}\tau_1} & \dots & e^{-j2\pi(-\frac{N_1-1}{2})f_{s,1}\tau_K} \\ \vdots & \ddots & \vdots \\ e^{-j2\pi(\frac{N_1-1}{2})f_{s,1}\tau_1} & \dots & e^{-j2\pi(\frac{N_1-1}{2})f_{s,1}\tau_K} \end{bmatrix} \in \mathbb{C}^{N_1 \times K},$$

$\boldsymbol{\beta} = [\alpha'_1, \dots, \alpha'_K]^T$, $\check{\mathbf{A}}$ and $\check{\boldsymbol{\beta}}$ have similar definitions. Then, we have the following theorem:

Theorem 2. $\check{\alpha}'_k = \alpha'_k$, $\check{\tau}_k = \tau_k$ is the unique solution of (37) if $N_1 + 1 > 2K$.

Proof: See [45], [46].

Apparently, the unique solution $\check{\alpha}'_k = \alpha'_k$, $\check{\tau}_k = \tau_k$ in (37) is also the unique solution for all identifiability equations in (36). Then, we prove that (36) has a unique solution: $\check{\varphi}'_m = \varphi'_m$. The identifiability equations of the m -th subband can be written as

$$\check{\Phi}\check{\mathbf{b}} = \Phi\mathbf{b}, \quad (38)$$

where $\mathbf{b} \in \mathbb{C}^{N_m \times 1}$ whose n -th element is $\sum_{k=1}^K \alpha'_k e^{-j2\pi f'_{e,m}\tau_k} e^{-j2\pi n f_{s,m}\tau_k}$, $\Phi = \text{diag}(e^{j\varphi'_m}, \dots, e^{j\varphi'_m}) \in \mathbb{C}^{N_m \times N_m}$, $\check{\Phi}$ and $\check{\mathbf{b}}$ have similar definitions. Due to the uniqueness of $\check{\alpha}'_k$ and $\check{\tau}_k$ proved as above, we have $\check{\mathbf{b}} = \mathbf{b}$. Hence, we have a unique solution of (38), i.e., $\check{\varphi}'_m = \varphi'_m$. Similarly, for identifiability equations of other subbands, the unique solution can also be guaranteed, i.e., $\check{\varphi}'_m = \varphi'_m$, $m = 2, \dots, M$, which completes the proof.

(ii) $\delta_m \neq 0, \forall m$. In this case, the signal model is ambiguous and the parameters to be estimated are non-identifiable. One approach to eliminate the ambiguity is to introduce a prior distribution of the parameters. In this way, the estimation problem becomes a Bayesian one. In our case, the parameter δ_m follows a prior distribution $p(\delta_m) \sim \mathcal{N}(0, \sigma_p^2)$, where σ_p is assumed to be small. Consequently, the prior information of δ is helpful to eliminate the ambiguity of signal model (4) and thus the estimation performance mainly depends on the prior information precision $(\sigma_p^2)^{-1}$.

In summary, when $\delta_m = 0, \forall m$, the parameters to be estimated in (4) are identifiable under a condition that $N_1 + 1 > 2K$. When $\delta_m \neq 0, \forall m$, though the parameters to be estimated in (4) are non-identifiable, the prior information of δ can help to eliminate the ambiguity of signal model (4). The sensing performance can still be guaranteed with a small σ_p .

B. Elements in (9)

We define $\bar{\mathbf{J}}_w = \mathbb{E}_{\mathbf{y}} \left[-\frac{\partial^2 \ln f(\mathbf{y}|\boldsymbol{\eta})}{\partial \boldsymbol{\eta} \partial \boldsymbol{\eta}^T} \right]$, whose elements are given by

$$\bar{\Psi}(x_r, x_s) = \frac{2}{\sigma_{ns}^2} \sum_{m,n} \text{Re} \left\{ \frac{\partial \boldsymbol{\mu}^H}{\partial x_r} \frac{\partial \boldsymbol{\mu}}{\partial x_s} \right\}. \quad (39)$$

Then, the elements of \mathbf{J}_w are obtained by taking the expectation of $\bar{\mathbf{J}}_w$ over the random parameter δ . Besides, the FIM \mathbf{J}_p is given by

$$\mathbf{J}_p = \text{diag} \left(0, \dots, 0, 1/\sigma_p^2, \dots, 1/\sigma_p^2 \right), \quad (40)$$

where only the diagonal elements associated with the position of block matrix $\Psi(\boldsymbol{\delta}, \boldsymbol{\delta})$ are non-zero. Finally, based on (8), (39), and (40), the entries of \mathbf{J}_η are given by

$$\begin{aligned}
\Psi(\tau_r, \tau_s) &= \frac{8\pi^2}{\sigma_{ns}^2} \sum_{m,n} f_{m,n}^2 \operatorname{Re} \left\{ (\alpha'_r)^* \alpha'_s e^{j2\pi f_{m,n}(\tau_r - \tau_s)} \right\}, \\
\Psi(\tau_r, \alpha_{R,s}) &= \frac{4\pi}{\sigma_{ns}^2} \sum_{n,m} \operatorname{Re} \left\{ j f_{m,n} (\alpha'_r)^* e^{j2\pi f_{m,n}(\tau_r - \tau_s)} \right\}, \\
\Psi(\tau_r, \alpha_{I,s}) &= \frac{-4\pi}{\sigma_{ns}^2} \sum_{n,m} \operatorname{Re} \left\{ f_{m,n} (\alpha'_r)^* e^{j2\pi f_{m,n}(\tau_r - \tau_s)} \right\}, \\
\Psi(\tau_r, \varphi'_i) &= -\frac{4\pi}{\sigma_{ns}^2} \sum_{n,m=i} \operatorname{Re} \left\{ f_{i,n} (\alpha'_r)^* \sum_{k=1}^K \alpha'_k e^{j2\pi f_{i,n}(\tau_r - \tau_k)} \right\}, \\
\Psi(\tau_r, \delta_i) &= \frac{8\pi^2}{\sigma_{ns}^2} \sum_{n,m=i} n f_{i,n} f_{s,i} \operatorname{Re} \left\{ (\alpha'_r)^* \sum_{k=1}^K \alpha'_k e^{j2\pi f_{i,n}(\tau_r - \tau_k)} \right\}, \\
\Psi(\alpha_{R,r}, \alpha_{R,s}) &= \Psi(\alpha_{I,r}, \alpha_{I,s}) \\
&= \frac{2}{\sigma_{ns}^2} \sum_{m,n} \cos(2\pi f_{m,n}(\tau_r - \tau_s)), \\
\Psi(\alpha_{R,r}, \alpha_{I,s}) &= -\Psi(\alpha_{I,r}, \alpha_{R,s}) \\
&= -\frac{2}{\sigma_{ns}^2} \sum_{m,n} \sin(2\pi f_{m,n}(\tau_r - \tau_s)), \\
\Psi(\alpha_{R,r}, \varphi'_i) &= \frac{2}{\sigma_{ns}^2} \sum_{n,m=i} \operatorname{Re} \left\{ j \sum_{k=1}^K \alpha'_k e^{j2\pi f_{i,n}(\tau_r - \tau_k)} \right\}, \\
\Psi(\alpha_{R,r}, \delta_i) &= -\frac{4\pi}{\sigma_{ns}^2} \sum_{n,m=i} \operatorname{Re} \left\{ j n f_{s,i} \sum_{k=1}^K \alpha'_k e^{j2\pi f_{i,n}(\tau_r - \tau_k)} \right\}, \\
\Psi(\alpha_{I,r}, \varphi_i) &= \frac{2}{\sigma_{ns}^2} \sum_{n,m=i} \operatorname{Re} \left\{ \sum_{k=1}^K \alpha'_k e^{j2\pi f_{i,n}(\tau_r - \tau_k)} \right\}, \\
\Psi(\alpha_{I,r}, \delta_i) &= -\frac{4\pi}{\sigma_{ns}^2} \sum_{n,m=i} \operatorname{Re} \left\{ n f_{s,i} \sum_{k=1}^K \alpha'_k e^{j2\pi f_{i,n}(\tau_r - \tau_k)} \right\}, \\
\Psi(\varphi'_r, \varphi'_s) &= \begin{cases} \frac{2}{\sigma_{ns}^2} \sum_{n,m=r} \left| \sum_{k=1}^K \alpha'_k e^{-j2\pi f_{r,n} \tau_k} \right|^2, & r = s \\ 0, & \text{otherwise,} \end{cases} \\
\Psi(\varphi'_r, \delta_s) &= \begin{cases} -\frac{4\pi}{\sigma_{ns}^2} \sum_{n,m=r} n f_{s,r} \left| \sum_{k=1}^K \alpha'_k e^{-j2\pi f_{r,n} \tau_k} \right|^2, & r = s \\ 0, & \text{otherwise,} \end{cases} \\
\Psi(\delta_r, \delta_s) &= \begin{cases} \frac{8\pi^2}{\sigma_{ns}^2} \sum_{n,m=r} n^2 f_{s,r}^2 \left| \sum_{k=1}^K \alpha'_k e^{-j2\pi f_{r,n} \tau_k} \right|^2 + \frac{1}{\sigma_p^2}, & r = s \\ 0, & \text{otherwise.} \end{cases}
\end{aligned} \tag{41}$$

C. The Compactly Reformulated FIM of (41)

The Dirichlet kernel is given by

$$s(x) = \sum_{n=-(N-1)/2}^{(N-1)/2} e^{jnx} = \frac{\sin\left(\frac{N}{2}x\right)}{\sin\left(\frac{1}{2}x\right)}. \quad (42)$$

We denote $\alpha'_k = a_k e^{j\phi_k}$, $\forall k$, where a_k and ϕ_k are the amplitude and phase of α'_k , respectively. Then the reformulated FIM can be derived based on (42), which is given by

$$\begin{aligned} \Psi(\tau_r, \tau_s) &= \frac{2}{\sigma_{ns}^2} \sum_{m=1}^M a_r a_s [4\pi^2 f_{c,m}^2 \cos(\psi_m - \Delta\phi) \gamma_m \\ &\quad + 4\pi f_{c,m} \sin(\psi - \Delta\phi) \gamma'_m - \cos(\psi_m - \Delta\phi) \gamma''_m], \\ \Psi(\tau_r, \alpha_{R,s}) &= \frac{2}{\sigma_{ns}^2} \sum_{m=1}^M 2\pi a_r f_{c,m} \sin(\psi_m + \phi_r) \gamma_m \\ &\quad - a_r \cos(\psi_m + \phi_r) \gamma'_m, \\ \Psi(\tau_r, \alpha_{I,s}) &= \frac{2}{\sigma_{ns}^2} \sum_{m=1}^M -2\pi a_r f_{c,m} \cos(\psi_m + \phi_r) \gamma_m \\ &\quad - a_r \sin(\psi_m + \phi_r) \gamma'_m, \\ \Psi(\alpha_{R,r}, \alpha_{R,s}) &= \Psi(\alpha_{I,r}, \alpha_{I,s}) = \frac{2}{\sigma_{ns}^2} \sum_{m=1}^M \cos(\psi_m) \gamma_m, \\ \Psi(\alpha_{R,r}, \alpha_{I,s}) &= -\Psi(\alpha_{R,s}, \alpha_{I,r}) = \frac{2}{\sigma_{ns}^2} \sum_{m=1}^M \sin(\psi_m) \gamma_m, \\ \Psi(\tau_r, \varphi'_2) &= -\frac{2}{\sigma_{ns}^2} [2\pi f_{c,2} (a_r^2 N_2 + a_1 a_2 \cos(\psi_2 - \Delta\phi) \gamma_2) \\ &\quad + a_1 a_2 \sin(\psi_2 - \Delta\phi) \gamma'_2], \\ \Psi(\alpha_{R,r}, \varphi'_m) &= \frac{2}{\sigma_{ns}^2} (-N_m a_r \sin(\phi_r) \\ &\quad - a_s \sin(\psi_m + \phi_s) \gamma_m), \quad r = 1, 2; s \neq r, \\ \Psi(\alpha_{I,r}, \varphi'_m) &= \frac{2}{\sigma_{ns}^2} (N_m a_r \cos(\phi_r) + a_s \cos(\psi_m + \phi_s) \gamma_m), \\ \Psi(\varphi'_2, \varphi'_2) &= \frac{2}{\sigma_{ns}^2} (N_2 (a_1^2 + a_2^2) + a_1 a_2 \gamma_2 (\cos(\psi_2 + \phi_1) \\ &\quad + \cos(\psi_2 - \phi_2))), \\ \Psi(\varphi'_2, \delta_2) &= \frac{2}{\sigma_{ns}^2} (-a_1 a_2 \gamma'_m (\sin(\psi_m + \phi_1) + \sin(\psi_m - \phi_2))), \end{aligned}$$

$$\begin{aligned}
\Psi(\tau_r, \delta_m) &= \frac{2}{\sigma_{ns}^2} (4\pi^2 a_r^2 f_{s,m}^2 \frac{N_m^3 - N_m}{12} - a_1 a_2 \\
&\quad \times [6\pi f_{c,m} \sin(\psi_m - \Delta\phi) \gamma'_m + \cos(\psi_m - \Delta\phi) \gamma''_m]), \\
\Psi(\alpha_{R,r}, \delta_m) &= \frac{2}{\sigma_{ns}^2} (-a_s \cos(\psi_m + \phi_s) \gamma'_m), \\
\Psi(\alpha_{I,r}, \delta_m) &= \frac{2}{\sigma_{ns}^2} (-a_s \sin(\psi_m + \phi_s) \gamma'_m), \\
\Psi(\delta_m, \delta_m) &= \frac{2}{\sigma_{ns}^2} [4\pi^2 (a_1^2 + a_2^2) \frac{N_m^3 - N_m}{12} f_{s,m}^2 - a_1 a_2 \gamma''_m \\
&\quad \times (\cos(\psi_m + \phi_1) + \cos(\psi_m - \phi_2))] + \frac{1}{\sigma_p^2},
\end{aligned} \tag{43}$$

where $\gamma_m = \frac{\sin(\pi N_m f_{s,m} \Delta\tau)}{\sin(\pi f_{s,m} \Delta\tau)}$, $\gamma'_m = \frac{\partial \gamma_m}{\partial \Delta\tau}$, $\gamma''_m = \frac{\partial^2 \gamma_m}{\partial (\Delta\tau)^2}$, $\psi_m = 2\pi f_{c,m} \Delta\tau$, and $\Delta\phi = \phi_2 - \phi_1$.

D. The derivation for CRB_{up} and CRB_{low} in (14)

First, we present the closed-form expression of $C_{\Delta\tau}$, which is given by

$$C_{\Delta\tau}(t) \triangleq f(t) = \frac{a + bt}{ct^2 + dt + e}, \tag{44}$$

where $t = \cos(2\pi \Delta f_c \Delta\tau) \in [-1, 1]$ is a carrier term, a, b, c, d, e are intricate coefficients given by

$$\begin{aligned}
a &= 12\bar{N}^2 - 6\gamma^2, \\
b &= -6\gamma^2, \\
c &= -3\gamma^2\gamma'' + 3\gamma\gamma'^2, \\
d &= 6\pi^2 \Delta f_c^2 \gamma^3 + (-2\bar{N}^3 \pi^2 f_s^2 + 2\bar{N} \pi^2 f_s^2 - 6\gamma'')\gamma^2 \\
&\quad + (-6\bar{N}^2 \pi^2 \Delta f_c^2 + 6\gamma'^2)\gamma + 6\bar{N}^2 \gamma'' - 6\bar{N} \gamma'^2, \\
e &= 4\bar{N}^5 \pi^2 f_s^2 + \pi^2 (-2f_s^2 \gamma^2 + 12\Delta f_c^2 - 4f_s^2) \bar{N}^3 + (-6\pi^2 \Delta f_c^2 \gamma + 6\gamma'') \bar{N}^2 \\
&\quad + ((-12\Delta f_c^2 + 2f_s^2)\gamma^2 \pi^2 - 6\gamma'^2) \bar{N} - 3\gamma^2 \gamma'' + 3\gamma\gamma'^2,
\end{aligned}$$

When $\bar{N} \rightarrow \infty$, from the expressions of γ, γ' , and γ'' , it can be shown that γ, γ' , and γ'' are bounded. Hence, when $\bar{N} f_s \Delta\tau$ is not an integer, we have $\gamma \neq 0$ and

$$f(t) = \frac{a}{\bar{d}t + e} + \varepsilon(\bar{N}), \tag{45}$$

where $\bar{d} = -2\bar{N}^3 \pi^2 f_s^2 \gamma^2 < 0$ and $\frac{\varepsilon(\bar{N})(\bar{d}t + e)}{a} \rightarrow 0$ as $\bar{N} \rightarrow \infty$. Therefore, $f(t)$ is a monotonic function for $t \in [-1, 1]$ when \bar{N} is sufficiently large and $\bar{N} f_s \Delta\tau$ is not an integer. Finally, the upper (lower) bound of $C_{\Delta\tau}$, i.e., CRB_{up} and CRB_{low} in (14), can be obtained by taking the values $t = \pm 1$.

E. Proof of Lemma 1

For the i -th iteration, we have $C_{\Delta\tau}(\boldsymbol{\xi}^i, \Delta\tau^i) \leq C_{\Delta\tau}(\boldsymbol{\xi}^{i-1}, \Delta\tau^i)$. This inequality holds because the adopted SCA algorithm starts from the initial point $\boldsymbol{\xi}^{i-1}, \Delta\tau^i$ and decreases $C_{\Delta\tau}(\boldsymbol{\xi})$ until converging to a stationary point of \mathcal{P}_2 . Then, we have

$$\sqrt{C_{\Delta\tau}(\boldsymbol{\xi}^i, \Delta\tau^i)} \leq \sqrt{C_{\Delta\tau}(\boldsymbol{\xi}^{i-1}, \Delta\tau^i)} \stackrel{a}{=} \Delta\tau^i, \quad (46)$$

where (46-a) holds due to that when we solve the problem \mathcal{P}_1 with $\boldsymbol{\xi} = \boldsymbol{\xi}^{i-1}$ to get the solution $\Delta\tau^i$, $(\boldsymbol{\xi}^{i-1}, \Delta\tau^i)$ must satisfy the equality constraint in \mathcal{P}_1 . Then, from the expression of CRB in (10) and the corresponding FIM expression (43), it can be shown that there always exists a sufficiently small number $\varepsilon_{\Delta\tau} > 0$ such that

$$\sqrt{C_{\Delta\tau}(\boldsymbol{\xi}^i, \varepsilon_{\Delta\tau})} > \varepsilon_{\Delta\tau}. \quad (47)$$

Next, based on (46) and (47), we have

$$(\sqrt{C_{\Delta\tau}(\boldsymbol{\xi}^i, \Delta\tau^i)} - \Delta\tau^i)(\sqrt{C_{\Delta\tau}(\boldsymbol{\xi}^i, \varepsilon_{\Delta\tau})} - \varepsilon_{\Delta\tau}) \leq 0. \quad (48)$$

Then, since $C_{\Delta\tau}$ is a continuous function and according to the Existence Theorem of Zero Points, we can obtain a zero point $\zeta \in (\varepsilon_{\Delta\tau}, \Delta\tau^i]$ satisfying the equality

$$\sqrt{C_{\Delta\tau}(\boldsymbol{\xi}^i, \zeta)} - \zeta = 0. \quad (49)$$

We know that $\Delta\tau^{i+1}$ is the global optimum of \mathcal{P}_1 at the $(i+1)$ -th iteration, which means that it is also the minimum zero point of (49). Hence, we finally have $\Delta\tau^{i+1} \leq \zeta \leq \Delta\tau^i$.

F. Proof of Theorem 1

We called $\boldsymbol{\xi}^*, \Delta\tau^*$ a stationary point of $\mathcal{P}_e/\mathcal{P}$ if it satisfies the KKT condition of \mathcal{P}_e , i.e., there exists μ_1, \dots, μ_J and λ such that

$$\nabla C_{\Delta\tau}(\boldsymbol{\xi}^*, \Delta\tau^*) + \sum_{j=1}^J \mu_j \nabla g_j(\boldsymbol{\xi}^*) + \lambda \nabla h(\boldsymbol{\xi}^*, \Delta\tau^*) = 0, \quad (50)$$

$$\mu_j g_j(\boldsymbol{\xi}^*) = 0, \forall j, \quad (51)$$

$$g_j(\boldsymbol{\xi}^*) \leq 0, \forall j, \quad (52)$$

$$\mu_j \geq 0, \forall j, \quad (53)$$

$$h(\boldsymbol{\xi}^*, \Delta\tau^*) = 0, \quad (54)$$

where ∇ denotes the gradient operator. Subsequently, we would like to prove that the limiting point $\boldsymbol{\xi}^*, \Delta\tau^*$ of the sequence $\{\boldsymbol{\xi}^i, \Delta\tau^i\}_{i=1}^{\infty}$ satisfies the KKT conditions (50)-(54).

For the i -th iteration, the stationary point of problem \mathcal{P}_2 obtained from the SCA algorithm satisfies the KKT

condition of \mathcal{P}_2 , i.e.,

$$\begin{aligned} \nabla C_{\Delta\tau}(\boldsymbol{\xi}^i, \Delta\tau^i) + \sum_{j=1}^J \tilde{\mu}_j \nabla g_j(\boldsymbol{\xi}^i) &= 0, \\ g_j(\boldsymbol{\xi}^i) &\leq 0, \forall j, \\ \tilde{\mu}_j &\geq 0, \forall j, \\ \tilde{\mu}_j g_j(\boldsymbol{\xi}^i) &= 0, \forall j. \end{aligned} \quad (55)$$

Let $\lambda = 0, \mu_j = \tilde{\mu}_j, \forall j$, according to (55), we have the limiting point $\boldsymbol{\xi}^*, \Delta\tau^*$ satisfying the KKT conditions (50)-(53) of problem \mathcal{P}_e . Then, we prove that the limiting point also satisfies the KKT condition (54). We have

$$\begin{aligned} \lim_{i \rightarrow \infty} \sqrt{C_{\Delta\tau}(\boldsymbol{\xi}^i, \Delta\tau^i)} &\stackrel{a}{=} \lim_{i \rightarrow \infty} \sqrt{C_{\Delta\tau}(\boldsymbol{\xi}^i, \Delta\tau^{i+1})} \\ &= \lim_{i \rightarrow \infty} \Delta\tau^{i+1} \\ &\stackrel{b}{=} \Delta\tau^i, \end{aligned} \quad (56)$$

where (56-a) and (56-b) follow from the continuity of function $\sqrt{C_{\Delta\tau}(\boldsymbol{\xi}, \Delta\tau)}$ and (34). Therefore, following from (56), the limiting point $\boldsymbol{\xi}^*, \Delta\tau^*$ of the sequence $\{\boldsymbol{\xi}^i, \Delta\tau^i\}_{i=1}^{\infty}$ satisfies the KKT condition (54), which completes the proof.

REFERENCES

- [1] M. Youssef, M. Mah, and A. Agrawala, "Challenges: Device-free passive localization for wireless environments," in *Proc. 13th Annu. ACM Int. Conf. Mobile Comput. Netw. (MobiCom)*, Sep. 2007, pp. 222–229. [Online]. Available: <https://doi.org/10.1145/1287853.1287880>
- [2] J. Shen, A. F. Molisch, and J. Salmi, "Accurate passive location estimation using TOA measurements," *IEEE Trans. Wireless Commun.*, vol. 11, no. 6, pp. 2182–2192, Jun. 2012.
- [3] D. Wu, D. Zhang, C. Xu, H. Wang, and X. Li, "Device-free WiFi human sensing: From pattern-based to model-based approaches," *IEEE Commun. Mag.*, vol. 55, no. 10, pp. 91–97, Oct. 2017.
- [4] B. Tan, Q. Chen, K. Chetty, K. Woodbridge, W. Li, and R. Piechocki, "Exploiting WiFi channel state information for residential healthcare informatics," *IEEE Commun. Mag.*, vol. 56, no. 5, pp. 130–137, May. 2018.
- [5] Z. Zhou, Z. Yang, C. Wu, L. Shanguan, and Y. Liu, "Omnidirectional coverage for device-free passive human detection," *IEEE Trans. Parallel Distrib. Syst.*, vol. 25, no. 7, pp. 1819–1829, Jul. 2014.
- [6] B. Paul, A. R. Chiriyath, and D. W. Bliss, "Survey of RF communications and sensing convergence research," *IEEE Access*, vol. 5, pp. 252–270, 2017.
- [7] D. K. Pin Tan, J. He, Y. Li, A. Bayesteh, Y. Chen, P. Zhu, and W. Tong, "Integrated sensing and communication in 6G: Motivations, use cases, requirements, challenges and future directions," in *Proc. 1st IEEE Int. Online Symp. Joint Commun. Sens.*, Feb. 2021, pp. 1–6.
- [8] A. Liu, Z. Huang, M. Li, Y. Wan, W. Li, T. X. Han, C. Liu, R. Du, D. K. P. Tan, J. Lu, Y. Shen, F. Colone, and K. Chetty, "A survey on fundamental limits of integrated sensing and communication," *IEEE Commun. Surveys Tuts.*, vol. 24, no. 2, pp. 994–1034, 2nd Quart. 2022.
- [9] D. Vasisht, S. Kumar, and D. Katabi, "Decimeter-level localization with a single WiFi access point," in *Proc. 13th Conf. Netw. Syst. Design Implement. (NSDI)*, Mar. 2016, pp. 165–178.
- [10] M. B. Khalilsarai, S. Stefanatos, G. Wunder, and G. Caire, "WiFi-based indoor localization via multi-band splicing and phase retrieval," in *Proc. IEEE 20th Int. Workshop Signal Process. Adv. Wireless Commun. (SPAWC)*, Jul. 2019, pp. 1–5.
- [11] M. B. Khalilsarai, B. Gross, S. Stefanatos, G. Wunder, and G. Caire, "WiFi-based channel impulse response estimation and localization via multi-band splicing," in *Proc. IEEE Global Commun. Conf. (GLOBECOM)*, Dec. 2020, pp. 1–6.
- [12] T. Kazaz, G. J. M. Janssen, J. Romme, and A.-J. van der Veen, "Delay estimation for ranging and localization using multiband channel state information," *IEEE Trans. Wireless Commun.*, vol. 21, no. 4, pp. 2591–2607, Apr. 2022.

- [13] Y. Wan, A. Liu, Q. Hu, M. Zhang, and Y. Cai, "Multiband delay estimation for localization using a two-stage global estimation scheme," *arXiv:2206.09751*, 2022. [Online]. Available: <https://doi.org/10.48550/arXiv.2206.09751>
- [14] M. Noschese, F. Babich, M. Comisso, and C. Marshall, "Multi-band time of arrival estimation for long term evolution (LTE) signals," *IEEE Trans. Mobile Comput.*, vol. 20, no. 12, pp. 3383–3394, Dec. 2021.
- [15] Y. Xie, Z. Li, and M. Li, "Precise power delay profiling with commodity Wi-Fi," *IEEE Trans. Mobile Comput.*, vol. 18, no. 6, pp. 1342–1355, Jun. 2019.
- [16] A. T. Mariakakis, S. Sen, J. Lee, and K.-H. Kim, "Sail: Single access point-based indoor localization," in *Proc. 12th Annu. Int. Conf. Mobile Syst. Appl. Services*, Jun. 2014, pp. 315–328. [Online]. Available: <https://doi.org/10.1145/2594368.2594393>
- [17] H. Rahul, H. Hassanieh, and D. Katabi, "SourceSync: A distributed wireless architecture for exploiting sender diversity," in *Proc. ACM SIGCOMM*, 2010, pp. 171–182. [Online]. Available: <https://doi.org/10.1145/1851182.1851204>
- [18] M. Pourkhaatoun and S. A. Zekavat, "Concatenated spectrum multi-band TOA estimation," in *Proc. 2011 IEEE Int. Symp. Pers. Indoor Mobile Radio Commun.*, Sep. 2011, pp. 1192–1196.
- [19] S. Smith, "Statistical resolution limits and the complexified Cramer-Rao bound," *IEEE Trans. Signal Process.*, vol. 53, no. 5, pp. 1597–1609, May. 2005.
- [20] H. Dun, C. C. J. M. Tiberius, C. Diouf, and G. J. M. Janssen, "Sparse signal bands selection for precise time-based ranging in terrestrial positioning," in *Proc. IEEE/ION Position Location Navigation Symp.*, Apr. 2020, pp. 1372–1380.
- [21] U. Oktel and R. Moses, "A bayesian approach to array geometry design," *IEEE Transactions on Signal Processing*, vol. 53, no. 5, pp. 1919–1923, May. 2005.
- [22] K. Suwa, M. Iwamoto, and T. Wakayama, "Analysis on the resolution of polarimetric radar and performance evaluation of the polarimetric bandwidth extrapolation method," *IEEE Trans. Geosci. Remote Sensing*, vol. 51, no. 7, pp. 4260–4278, Jul. 2013.
- [23] B. M. Sadler, N. Liu, and Z. Xu, "Ziv-Zakai bounds on time delay estimation in unknown convolutive random channels," *IEEE Trans. Signal Process.*, vol. 58, no. 5, pp. 2729–2745, May. 2010.
- [24] V. M. Chiriac, Q. He, A. M. Haimovich, and R. S. Blum, "Ziv-Zakai bound for joint parameter estimation in MIMO radar systems," *IEEE Trans. Signal Process.*, vol. 63, no. 18, pp. 4956–4968, Sep. 2015.
- [25] K. Bell, Y. Steinberg, Y. Ephraim, and H. Van Trees, "Extended Ziv-Zakai lower bound for vector parameter estimation," *IEEE Trans. Inform. Theory*, vol. 43, no. 2, pp. 624–637, Mar. 1997.
- [26] C. See and A. Gershman, "Direction-of-arrival estimation in partly calibrated subarray-based sensor arrays," *IEEE Transactions on Signal Processing*, vol. 52, no. 2, pp. 329–338, Feb. 2004.
- [27] P. Stoica and T. Marzetta, "Parameter estimation problems with singular information matrices," *IEEE Trans. Signal Process.*, vol. 49, no. 1, pp. 87–90, Jan. 2001.
- [28] H. L. V. Trees, *Detection, Estimation and Modulation Theory*. New York: Wiley, 1968, vol. 1.
- [29] P. Tichavsky, C. Muravchik, and A. Nehorai, "Posterior cramer-rao bounds for discrete-time nonlinear filtering," *IEEE Transactions on Signal Processing*, vol. 46, no. 5, pp. 1386–1396, May. 1998.
- [30] Y. Shen and M. Z. Win, "Fundamental limits of wideband localization - part I: A general framework," *IEEE Trans. Inform. Theory*, vol. 56, no. 10, pp. 4956–4980, Oct. 2010.
- [31] W. M. A., *Inverting modified matrices*. Memorandum Report 42, Statistical ResearchGroup, NJ: Princeton, 1950.
- [32] N. Liu, Z. Xu, and B. M. Sadler, "Ziv-zakai time-delay estimation bounds for frequency-hopping waveforms under frequency-selective fading," *IEEE Trans. Signal Process.*, vol. 58, no. 12, pp. 6400–6406, Dec. 2010.
- [33] H. L. V. Trees and K. L. Bell, *Bayesian Bounds for Parameter Estimation and Nonlinear Filtering/Tracking*. New York, NY, USA: Wiley, 2007.
- [34] R. Du, H. Xie, M. Hu, Narengerile, Y. Xin, S. McCann, M. Montemurro, T. X. Han, and J. Xu, "An overview on IEEE 802.11bf: WLAN sensing," *arXiv:2207.04859*, 2022. [Online]. Available: <https://arxiv.org/abs/2207.04859>
- [35] Z. Hu, A. Liu, Y. Wan, T. X. Han, and M. Zhao, "Stochastic particle-based variational bayesian inference for multi-band radar sensing," *arXiv:2207.10427*, 2022. [Online]. Available: <https://arxiv.org/abs/2207.10427>
- [36] Y.-F. Li, I. Tsang, J. Kwok, and Z.-H. Zhou, "Tighter and convex maximum margin-clustering." *Journal of Machine Learning Research - Proceedings Track*, vol. 5, pp. 344–351, Jan. 2009.
- [37] P.-C. Wang and J.-F. Tsai, "Global optimization of mixed-integer nonlinear programming for engineering design problems," in *in 2011 Int. Conf. System Science and Engineering*, Jun. 2011, pp. 255–259.

- [38] C. Jia, Y. Zhang, Y. Zeng, and C. Yuan, "An improved particle swarm optimization algorithm for solving mixed integer programming problems," in *2015 7th International Conference on Intelligent Human-Machine Systems and Cybernetics*, vol. 2, Aug. 2015, pp. 472–475.
- [39] M. Waheed and A. Cai, "Evolutionary algorithms for radio resource management in cognitive radio network," in *2009 IEEE 28th International Performance Computing and Communications Conference (IPCCC)*, Dec. 2009, pp. 431–436.
- [40] P. Lin and T. Lin, "Optimal dynamic spectrum access in multi-channel multi-user cognitive radio networks," in *Proc.IEEE PIMRC*, Sep. 2010, pp. 1637–1642.
- [41] L. Zhang, Y.-C. Liang, and Y. Xin, "Joint admission control and power allocation for cognitive radio networks," in *Proc.IEEE WCNC*, vol. 3, Apr. 2007, pp. III–673–III–676.
- [42] A. Liu, V. K. N. Lau, and M.-J. Zhao, "Online successive convex approximation for two-stage stochastic nonconvex optimization," *IEEE Trans. Signal Process.*, vol. 66, no. 22, pp. 5941–5955, Nov. 2018.
- [43] M. Razaviyayn, "Successive convex approximation: Analysis and applications," Ph.D. dissertation, Univ. Minnesota., 2014.
- [44] D. P. Bertsekas, *Nonlinear Programming*. Belmont, MA: Athena Scientific, 1995.
- [45] A. Nehorai, D. Starer, and P. Stoica, "Direction-of-arrival estimation in applications with multipath and few snapshots," *Circuits Syst. Signal Process.*, vol. 10, no. 3, pp. 327–342, May. 1991. [Online]. Available: <https://doi.org/10.1007/BF01187549>
- [46] J. Li, P. Stoica, L. Xu, and W. Roberts, "On parameter identifiability of MIMO radar," *IEEE Signal Process. Lett.*, vol. 14, no. 12, pp. 968–971, Dec. 2007.